2021

Correlating with Local Variation in Collagen Level and Mechanical Properties of the Heart Tissues

Talayeh Tavangar

CORRELATING WITH LOCAL VARIATION IN COLLAGEN LEVEL AND MECHANICAL PROPERTIES OF THE HEART TISSUES

_____

A Thesis

Presented to

the Faculty of the Daniel Felix Ritchie School of Engineering and Computer Science

University of Denver

_____

In Partial Fulfillment

of the Requirements for the Degree

Master of Science

_____

by

Talayeh Tavangar

June 2021

Advisor: Yun-Bo Yi

Author: Talayeh Tavangar
Title: CORRELATING WITH LOCAL VARIATION IN COLLAGEN LEVEL AND MECHANICAL PROPERTIES OF THE HEART TISSUES
Advisor: Yun-Bo Yi
Degree date: June 2021

ABSTRACT

The determination of the myocardium's tissue properties is essential in constructing finite element (FE) models of the heart. To obtain accurate results, especially for functionally modeling the heart, we must determine the tissue properties in-vivo. The calculation of the heart tissue properties remains a challenging area as it is categorized as a heterogeneous, anisotropic, nonlinear soft tissue that undergoes large deformation. In this work, we tried to introduce and evaluated a finite element method to determine the mechanical properties of the cardiac tissue. The introduced method combined a finite element modeling with the experimentally obtained images from the left and right ventricles to develop a model for calculating the shear modulus, Young's modulus, and the Poisson's ratio of the ventricles leading to obtaining the constitutive matrices for each specimen. Tissue behavior was quantified under three different loading conditions: tensile loading in the x and y direction and shear loading. Statistical analysis reveals that the left ventricle demonstrates higher mechanical properties compared to the right ventricle. Additionally, the heart tissue's mechanical properties were effectively used for studying the effects of the variation in the tissue's composition, primarily collagen, on the myocardium behavior. Based on the obtained results, it was demonstrated that mechanical properties enhanced with increasing the collagen amount. The results indicated that the proposed model showed a good agreement with the previous studies and provided an ability to describe the heart tissue's behavior precisely. It offers a new approach to the study of

cardiac tissue properties, as it shows the cardiac tissue's mechanical properties, including Young's modulus, shear modulus, constitutive matrices, and their correlation with the change in the microstructure of the heart tissue.

TABLE OF CONTENTS

LIST OF FIGURES

LIST OF TABLES

CHAPTER 1: INTRODUCTION

1.1 Motivation

Cardiovascular diseases remain the primary cause of death worldwide [26]. During the process of aging cardiac tissues undergo considerable stiffness changes, which may result in cardiac diseases caused by a restricted blood supply to the muscle, such as angina pectoris, myocardium infraction, cardiomyopathies, and heart failure [22,23]. For better diagnosis and evaluation of the risk factors in the patient with cardiac diseases, it is essential to obtain particular properties defining the passive and active mechanical properties of the heart tissue enabling us to construct biomechanical models and distinguish the differences between the functional features of a healthy and diseased heart [22]. The heart tissue consists of three distinct layers, including thin inner and outer layers and a thick middle layer, which is the myocardium [16]. The myocardium is primarily composed of cardiomyocytes arranged in bundles of muscle fibers, which change their orientations concerning their positions within the cells' wall [16]. Although it is viable to obtain the fibers' actual orientations and sheets in ex vivo heart myocardium, finding this data for in vivo situations has remained difficult [16]. Conventional methods that determined the properties of the myocardium using biaxial or uniaxial tests on specimens harvested from a specific heart section provide insight into formulating the myocardium's constitutive law. These methods have been proven to be practical tests in determining the general

Characteristics of cardiac tissue behavior in both healthy and diseased states. However, it is not sufficient to provide a unique description of the three-dimensional constitutive behavior of the myocardium. Several significant drawbacks arise from using uniaxial and biaxial tests, which are:

1. Variation in the values of the mechanical properties according to the experimental loading conditions. [20]
2. the mechanical properties of the heart change drastically after death. [20]
3. The properties may not be directly applicable for modeling the heart as the myocardium demonstrate heterogeneous behavior. [20]

All the above limitations led researchers to find different ways to run their experiments without using biaxial/uniaxial tests. An alternative method for obtaining accurate results is to use finite element analysis. Using FE combined with advanced simulation tools and medical imaging such as magnetic resonance imaging, computed tomography, and echocardiography where anatomy, motion, and flow can be imaged is a promising method for obtaining more accurate results [17,24]. Once the model is constructed, the desired outputs such as deformation behavior, wall stresses, and strains can be predicted from the model. It is essential to accurately use the human myocardium's passive biomechanical properties to simulate cardiac mechanics accurately in such models. Otherwise, the stress-strain prediction would lead to inaccurate diagnostic information [17,20].

In this project, we develop a method using the experimentally obtained images from the left and right ventricles and a finite element method to determine the heart tissue's mechanical properties. We also discussed the effects of the collagen variation on the cardiac tissue's mechanical properties as it is known that the mechanical and chemical properties of the heart tissue are highly related to collagen, and it varies as a function of distance from the heart [25]. This research's primary purpose is to develop a finite element procedure with MATLAB computer code to determine the Young's and shear modulus of the ventricles during the cardiac cycle. Based on the obtained results, the myocardium modulus can be effectively used as a valuable tool for understanding heart behavior and diagnosing its misfunction. [20]

1.2 Objectives

This thesis's objectives were to 1) characterize the material composition of the cardiac tissue and 2) develop a computational method to identify the mechanical properties of the heart tissue. A comprehensive model was developed to calculate the shear and Young's modulus and constitutive matrices of the ventricles, using experimentally obtained images from the previous study. Moreover, the results were used to find a correlation between the collagen amount's variation and the myocardium's behavior. Overall, this work's goal was to develop a suite of statistical and computational tools that provide an understanding of the anatomy and mechanical properties of cardiac tissue.

1.3 Organization

Chapter 2 provides an overview of the relevant clinical terminology and heart anatomy used in the subsequent chapters. In the last section of this chapter, we have gone through the previous studies and the methods used to calculate the heart tissue's mechanical properties.

Chapter 3 discusses the modeling approach to characterize the anatomic variability and the cardiac tissue's mechanical properties. Chapter 3 went through the steps and assumptions taken for modeling the heart tissue. Moreover, the methods used for the image processing of the images obtained from the left and right ventricles were discussed in this chapter.

Chapter 4 discusses the results obtained from the method developed in this study. The study employed finite element analysis to calculate the heart tissue's mechanical properties and examine the effects of the collagen variation on myocardium mechanical behavior. Chapter 4 presents the capabilities of a proposed procedure to predict the properties of cardiac tissue. This study provides valuable information on using the finite element method for analyzing the behavior of the ventricle.

Chapter 5 presents a summary of the work, discusses limitations, and makes recommendations for future research.

CHAPTER 2: LITERATURE REVIEW

This chapter presents an overview of the background information and literature pertinent to quantifying the heart tissue's mechanical properties and computational evaluation of heart mechanics. The first section goes through the heart's anatomy; the second and third sections describe the cardiac cycle and the heart's conduction systems. The fourth part describes the morphology of the heart wall. The fifth section provides a brief overview of the passive tissue behavior and the previous research for obtaining the heart tissue's mechanical properties. Clinical terminology and anatomy were obtained from "Biofluid Mechanics: The Human Circulation" by Krishnan B. Chandran and "Computational Hemodynamics-Theory, Modelling, and Applications" Jiyuan Tu and Kiao Inthavong. [1,2]

2.1 Anatomy of the Human Heart

The heart is one of the most critical organs in the human body; It is located within the thoracic cavity, medially between the lungs in the mediastinum space. [3] Within the mediastinum, the heart is separated from other mediastinal structures by a tough membrane known as the pericardium. [3] The heart's dorsal surface lies near the vertebrae's bodies, and its anterior surface sits deep to the sternum and costal cartilages. The great veins, the superior and inferior vein cavae, the great arteries, the aorta, and the pulmonary trunk are attached to the heart's superior surface at the third costal cartilage level. The heart's tip,

known as the apex, points toward the left side of the body and rests superior to the diaphragm [3].

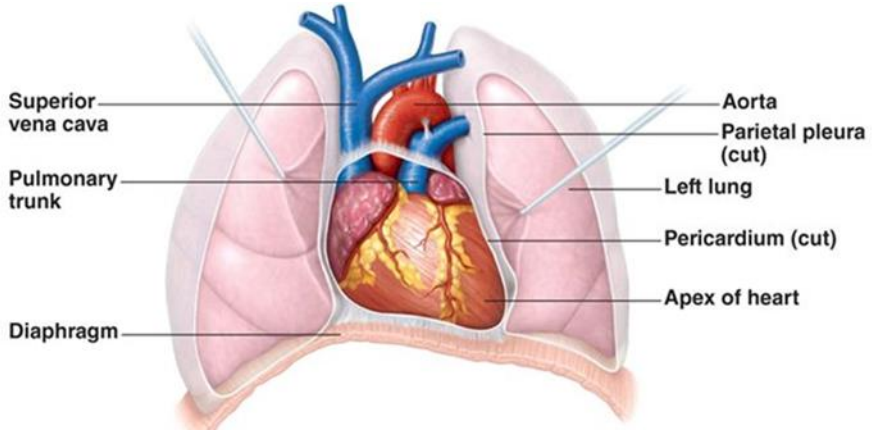

Figure2.1. ***Position of the Heart in the Thorax*** *The heart is located within the thoracic cavity, medially between the lungs in the mediastinum. It is about the size of a fist, is broad at the top, and tapers toward the base.[3*]

The heart's primary function is to supply oxygenated blood to the rest of the body and transport the de-oxygenated blood to the respiratory system, where carbon dioxide is excreted and oxygen is absorbed in the alveolar sac. In other words, the heart consists of two pumps in series circulating blood through the pulmonary and systemic circulations. The heart comprises the left and right atrium, separated by a muscular wall called septum; Each half consists of two chambers: a thin-walled atrium and a thick-walled ventricle. The atria and ventricles are responsible for receiving blood from the veins and pumping the blood out of the heart, respectively. The right atrium receives de-oxygenated blood collected from the whole body via two large veins called the superior and inferior vena cavea and then passes via the tricuspid valve to the right ventricle pumping the blood to the lungs through the pulmonary valve for oxygenation. The oxygenated blood returns to the heart via the pulmonary veins and is collected by the left atrium, which pumps the blood

into the left ventricle through the mitral valve. The left ventricle supplies the oxygenated blood into the systemic circulation via the aorta. [1,2]

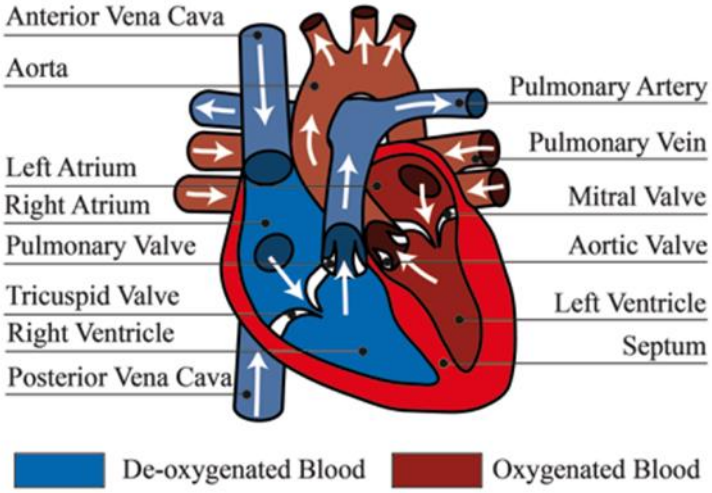

Figure 2.2. ***Cardiovascular circulation of the heart****. The heart comprises the left and right atria, which are responsible for collecting de-oxygenated and oxygenated blood from the vena cava and pulmonary vein, respectively. [2]*

The valves are responsible for unidirectional blood flow through the heart and the prevention of backflow. The heart consists of 4 valves: the aortic, Mitral valve, pulmonic, and tricuspid valve. The aortic valve is located at the base of the aorta, which prevents backflow from the aorta. It is usually composed of three flaps. When the ventricle relaxes and blood attempts to flow back into the ventricle from the aorta, blood will fill the valve's cusps. [3] The pulmonary valve is made of three small flaps of endothelium which are reinforced with connective tissue. When the ventricle relaxes, the difference in pressure causes blood to flow back into the ventricle from the pulmonary trunk. This flow of blood fills the pocket-like flaps of the pulmonary valve, causing the valve to close. Aortic and pulmonic valves are the same, although the pulmonic valve has lower peak velocities. The

Mitral valve consists of two cusps. While the aortic valve connects the left ventricle with the aorta, the mitral valve separates the left ventricle from the left atrium as it receives oxygenated blood from the lungs via the pulmonary vein. The tricuspid valve typically consists of three flaps, or leaflets, made of the endocardium reinforced with a flat sheet of dense connective tissue. The tricuspid valve's flow exhibits a similar velocity profile, although at lower speeds. [3,4]

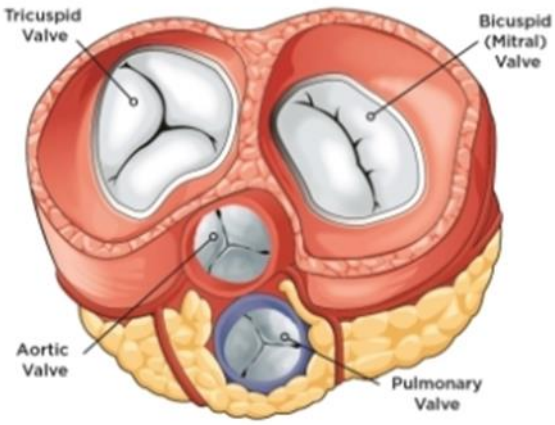

Figure 2.3. ***Heart Valves*** *With the atria and major vessels removed, all four valves are clearly visible, although it is difficult to distinguish the three separate cusps of the tricuspid valve. [3]*

2.1.1 The Physiology of the Coronary Arteries

The coronary arteries' primary responsibility is to deliver oxygenic blood to the heart tissue, which provided the energy required for the heart pumping. On the other hand, the cardiac veins transfer the de-oxygenated blood from the heart to the respiratory system. The coronary artery network includes the epicardial coronary arteries, which regulate blood supply to the heart tissue and are found on the heart's surface [2]. The left coronary artery distributes blood to the left side of the heart, the left atrium and ventricle, and the

interventricular septum. The circumflex artery arises from the left coronary artery and follows the coronary sulcus to the left. [3] The left anterior descending artery is the second major branch arising from the left coronary artery. It follows the anterior intervascular sulcus around the pulmonary trunk, which gives rise to many smaller units interconnecting with the posterior intervascular artery components resulting in the anastomoses. An anastomosis is an area where vessels are united to form interconnections making blood circulation possible. However, anastomoses in the heart are very small, which may result in coronary blockage. [3] The right coronary artery proceeds along the coronary sulcus and distributes blood to the right atrium, portions of both ventricles, and the heart conduction system. The marginal arteries that arise from the right coronary artery inferior to the right atrium supply blood to the right ventricle's superficial portions. The right coronary artery also supplies blood to the heart's posterior surface, giving rise to the posterior interventricular artery. [3]

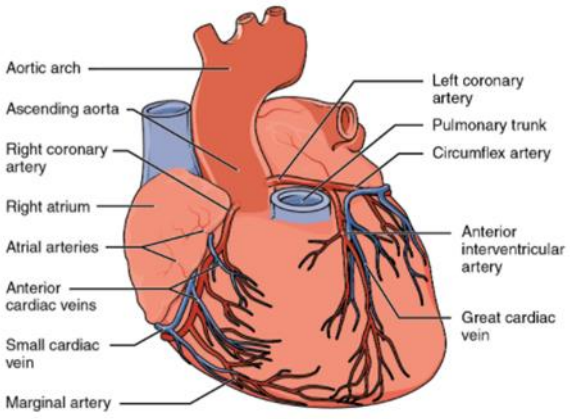

*Figure 2.4. Coronary **Circulation** The anterior view of the heart shows the prominent coronary surface vessels. [3]*

2.2 Cardiac cycle

The sequence of events that occur within one heartbeat is known as the cardiac cycle. The cardiac cycle is usually divided into two main phases, which are systole and diastole. During systole, the heart muscle transfers from its relaxed state to the instant of maximal mechanical activation. While during diastole, the heart muscle relaxes from the end-systolic state back towards its resting state. [2]

The mechanical events occurring during the cardiac cycle can be described as a series of changes in pressure in the ventricle chamber, causing blood to move in and out of the ventricle. As it was demonstrated in the following picture, shortly before time (A), left ventricle pressure (LVP) and left ventricle volume (LVV) are relatively constant, and aortic pressure (AoP) is gradually declining; During this time, the heart is in its diastolic state, and as the ejection of the blood into the atrial system, the aortic pressure falls. At the time (A), there is electrical activation of the heart, beginning contraction and rising pressure inside the chamber. Shortly after the contraction, (LVP) rises to be greater than left atrial pressure, and the mitral valve closes. Since (LVP) is less than aortic pressure, the aortic valve is closed. This state is known as isovolumic contraction, during which the ventricle is contracting isovolumically since both valves are closed, and no blood can enter or leave the ventricle. Eventually, at the time (B), (LVP) slightly exceeds (AoP), and the aortic valve opens. [7] Blood is ejected from the ventricle into the aorta during this time, and left ventricle volume decreases. As the cardiac muscle contraction process reaches its maximal effort, ejection slows down, and ultimately, as the muscles begin to relax, (LVP) falls below aortic pressure (time C), and the aortic valve closes. At this point, ejection has ended,

and the ventricle is at its lowest volume. [7] Eventually, (LVP) falls below the left atrium's pressure, and blood flows from the left atrium into the left ventricle as the mitral valve opens (time D). In general terms, systole and diastole include isovolumic contraction and ejection and isovolumic relaxation and filling. It turns out that there are many advantages to display (LVP) as a function of (LVV); The resulting pressure-volume diagram corresponding to the curve of the previous figure is shown below. This loop is called the pressure-volume loop. During the first part of the cycle, pressure rises, but the volume stays the same. The aortic valve opens at point (B), ejection begins, and volume decreases. After the ventricle reached its maximum activated state, (LVP) falls below (AoP), the aortic valve closes, and isovolumic relaxation commences. Finally, filling begins with the mitral valve opening at point (D). The above description is related to hemodynamic events occurring during the cardiac cycle in the left ventricle. The right ventricle events are similar, though occurring at slightly different times and different levels of pressure than in the left ventricle. [7]

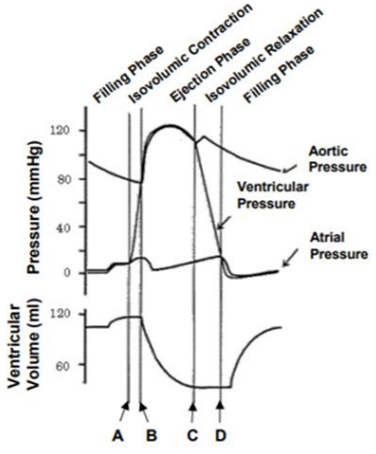

Figure 2.5. ***Overview of the Cardiac Cycle*** *The cardiac cycle begins with atrial systole*

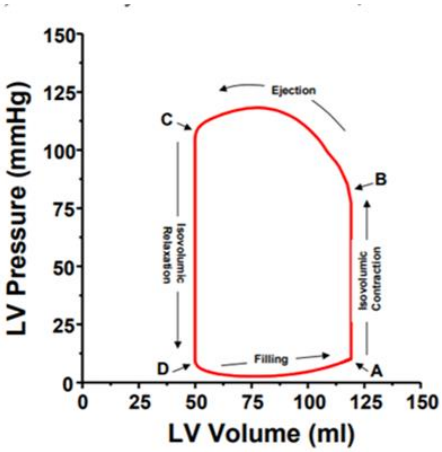

Figure 2.6. Pressure-volume loop during a cardiac cycle [7]

2.3 Conduction systems of the heart

The heart's conduction system consists of the myocardium and conducting fibers that initiate impulses and conduct them rapidly throughout the heart. The cardiac system is responsible for initiating and transmitting the electrical impulses related to each cardiac cycle's contractions. The conduction system can be divided into three main components: the sinoatrial (SA) nodes which are located in the right atrium, the atrioventricular (AV) nodes which are located on the inter-atrial septum, the His-Purkinje system located along the ventricle walls. [5] The SA node is the primary impulse initiator and regulator in the human heart. It is a flat, elliptical collection of specialized nodal tissue with dimensions of up to 25 millimeters in length. The node is nestled in the superior posterolateral wall of the right atrium near the superior vena cava's opening. The SA node is mainly populated with pale-staining cells known as cardiac pacemaker cells (P cells), primarily containing the central nucleus and a scant number of other organelles. Each heartbeat is initiated with an electrical potential generated in the SA node. [5]

This action spreads through the atrial muscle at a speed of about 0.3 m/s causing the muscles to contract and pump the blood through the atrioventricular valves into the ventricles. The AV node complex consists of junctional fibers, the node, transitional fibers, and the AV bundle; the AV bundle is the only pathway through which the electrical activity is conducted from the atrial to the ventricular chambers. A delay of about 110 ms occurred through the AV complex, allowing sufficient time for pumping the blood into the ventricles before ventricular contraction. The His bundle starts from the AV complex and has a large diameter. The His bundle conducts the electrical impulses into the ventricular muscles at a

speed of 1.5 to 2.5 m/s. The impulse enters the base of ventricles through His and then follows the left and right bundle branches, which results in fast depolarization and contraction of the heart muscle through the ventricles. [1, 6, 5]

2.4 Layers of the Heart Wall and Heart Muscle

The heart wall consists of three layers which are epicardium, myocardium, and endocardium. The middle and thickest layer is the myocardium, mainly made of cardiac muscle cells. It is built upon a framework of collagenous fibers, plus the blood vessels that supply the myocardium and the nerve fibers that help regulate the heart. [3] The myocardium can be divided into three major types: atrial, ventricular, and conducting muscle. The atrial and ventricular muscles contract due to electrical excitation, causing an increase in the blood pressure that induces the blood's pumping. The atrial and ventricular muscle consists of myofibrils containing actin and myosin filaments which slide across each other producing contraction. [3]

In comparison, the conductive muscle is responsible for conducting electrical activity to all parts of the heart. These fibers contain few contractile fibrils causing them to have a slight contraction. Each cardiac muscle cell is separated by an intercalated disc, giving the cardiac muscle a striated appearance. [1,8,3]

The epicardium is the heart's outermost layer made of mesothelial cells, which is the serous pericardium's visceral layer. Beneath the mesothelial cells is a layer of connective tissue that binds the epicardium to the myocardium. Nerves and blood vessels that transfer blood to the heart muscle exist in this part. The innermost layer of the heart

wall is the endocardium; it is joined to the myocardium with a thin layer of connective tissue; The endocardium lines the chambers where the blood circulates and covers the heart valves made of squamous epithelium named endothelium which is continuous with the endothelial lining of the blood vessels. [3]

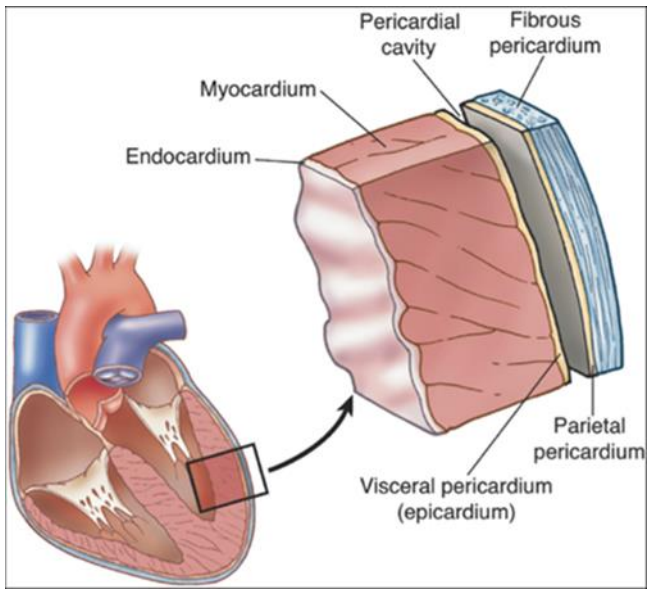

Figure 2.7. ***Pericardial Membranes and Layers of the Heart Wall*** *The pericardial membrane that surrounds the heart consists of three layers and the pericardial cavity. The heart wall also consists of three layers. The pericardial membrane and the heart wall share the epicardium. [3]*

2.4.1 Morphology of the myocardial

The myocardial muscle, also called cardiac muscle, is one of the three major muscle types. The other two muscle types are skeletal muscle and smooth muscle. The structure of cardiac muscle shares some features with skeletal muscle but has many distinctive features. Cardiac muscle is shorter than skeletal muscle and has fewer nuclei. It is composed of tubular muscle called myocytes, which consists of many chains of myofibrils. Myofibrils are also made of contractile units known as sarcomeres. Each sarcomere is composed of

two prominent filaments: thick myosin and thin actin filaments, which are the active structures sliding past each other during contraction and relaxation of the cardiac muscle. [5,28]

Myocardial muscle cells are arranged in parallel bundles joined to each other at the intercalated disc regions at the end and along the cells' side. Since the adjusted myocytes are almost aligned parallel, a mean myocytes axis vector can be defined at any point, referred to as the mean fiber orientation. [5] Fiber orientation undergoes an orderly transition from the epicardium to the endocardium in the left ventricle, with circumferential fibers predominating in the middle one-third of the heart wall. In general, muscle fibers' orientation within the left ventricular subendocardium is vertical, running from base to apex, with parallel fibers within both ventricles' papillary muscles and trabecular muscles. Successively deeper layers in the left ventricle from the endocardium are oriented more horizontally, with fibers in the mid-wall region approximately 70 to 90 degrees to those of the subendocardium. [27] At the subepicardial, fibers have turned roughly 120 degrees from those in the subendocardium. Myocytes' bundles comprise the laminar structure and orientation, allowing the translation of individual cardiomyocytes' contraction to torsion and twist to complete ventricular contraction. This laminar orientation comprises a perimysium composed of a bundle of collagen fibers that connect the epimysium to the endomysium. The endomysium has at least four components: a dense weave network surrounding myocytes, myocyte–myocyte collagen struts that connect adjacent myocytes, myocyte–capillary struts connect capillaries and myocytes, and a complex of single

collagen fibers, glycoproteins, and glycosaminoglycans. The amount of collagen in each component varies with the function of the muscle. [11,27, 28]

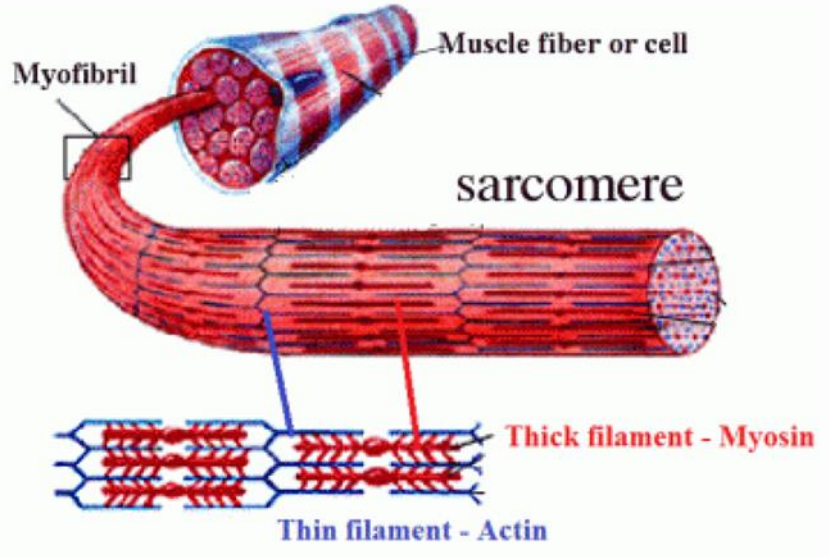

Figure 2.8. Morphology of the myocardial [28]

2.5 Characteristics of the Passive Tissue

The cardiac muscle can be described as a non-homogenous, orthotropic, and incompressible material. Heart muscle can be considered as a viscoelastic material as it shows stress relaxation under-maintained stretch, creeping under-maintained stress, and hysteresis in cyclic loading. However, since the viscoelastic response's relaxation time is longer than the cardiac cycle, viscoelasticity is not crucial in the material's mechanical modeling. [5]

The constitutive equation gives information about the materials' responses to stresses. Choosing an appropriate constitutive equation depends on the materials' properties, the magnitude of stress change, and the loading rate. We can describe most of

the materials around us with one of the three idealized, simplified stress-strain relationships: Newtonian fluid, non-Newtonian fluid, and elastic materials. However, most biological materials, including soft tissue, cannot be categorized as one of the above materials, and a more complex equation is needed to describe their behavior under applied stresses. There are two approaches for formulating the soft tissue's constitutive equation: structural and phenomenological approaches. In phenomenological approaches, researchers try to fit a mathematical equation to the obtained experimental data. However, in the structural approach, the material's microscopic structure is considered, and parameters in the equation are calculated by considering the material's morphology and structure. In the following paragraphs, we discuss the studies done by the previous scientists for obtaining the constitute equation for cardiac tissue. [5]

The cardiac muscle exhibits complex geometry, large deformation, and heterogeneity of the structure, making it complex to obtain the myocardium's mechanical properties. In the past decades, existed information regarding heart tissue properties was barely based on results gained from uniaxial experiments; Since most of the heart tissues were subjected to multiaxial loads, the result from uniaxial testing did not accurately reflect the actual stresses-strain distributions in the heart walls. Furthermore, uniaxial data cannot be generalized to provide a three-dimensional property [12]. So, Demar et al. used multiaxial loading conditions for determining the three-dimensional mechanics of the myocardium. Although their research was an outstanding achievement in order to obtain accurate results for passive mechanical properties of heart myocardium; There are some drawbacks regarding their experiment method, which are as follow: they used individual

strands of silk while allowing free lateral motion, which produced tears in the tissue, they assumed that the same amount of tension was applied in each strand which is hardly achieved. Finally, they used a support needle which produced some restrain to free lateral motion due to the friction between the tissue and the needle. Hence, the absolute values of stiffness were likely over-estimated, making their results unreliable to use for diagnosis [12]. V.P. Novak et al. took the same approach and used in vitro biaxial experiment on 28 thin, rectangular slabs of the myocardium for determining the mechanical behavior of passive myocardium in distinct regions of the heart. However, they calculated W, which represents the energy stored in a material during deformation, to describe the heart myocardium's constitutive relations [13]. W was calculated by using the following equation:

$$W = c_1(\alpha - 1)^2 + c_2(\alpha - 1)^3 + c_3(I_1 - 3) + c_4(I_1 - 3)(\alpha - 1) + c_5(I_1 - 3)^2 \qquad (2.1)$$

I_1 and α are the coordinate's invariant measure of the deformation, and C_k are the materials parameters. The best-fit values of the five materials parameters were determined by minimizing the error between experimental data and theoretical biaxial stresses. Then, they calculated the values of W for equiaxial and uniaxial stretches. The results of their experiment emphasized that the myocardium exhibits anisotropic behavior. Besides, they found out that despite the regional differences in the strain-energy stored during deformation, outer and inner portions of the left ventricle free wall tended to be stiffer than the left ventricle middle wall [13]. There are also some limitations regarding their research, including they only tested restricted sites of left ventricles since the curvature of the left ventricles makes it challenging to obtain large specimens. Because of the nonlinear cardiac

tissue behavior, even a slight discrepancy in material properties used for the stress calculations may result in significant errors making their result unstable. [13]

Results obtained from mentioned simple bi-axial testing demonstrated the anisotropic solid behavior of the myocardium. Although some aspects of the myocardium's passive mechanical responses were well characterized using these methods, more accurate methods need to be used for detailed materials parameter estimations for constative laws used to model the human myocardium. [14]

Holzapfel et al. [15] proposed a structure-based constitutive model of myocardium that accounts for the locally anisotropic tissue by expressing the strain energy functional using fiber-based material invariants. This model is very reliable and can fit almost all the experimental data. So, we will focus on this model in the following sections. In this model, strain energy function (ϕ) for myocardium is calculated from the following equation:

$$\varphi = \frac{a}{2b} e^{b(I_1-3)} + \sum \frac{a_i}{2b_i} \left[e^{b_i(I_{4i}-1)^2} - 1\right] + \frac{a_{fs}}{2b_{fs}} \left[e^{b_{fs}I_{8fs}} - 1\right] \quad (2.2)$$

Where a, b are parameters for the matrix responses; a_f, and b_f are the parameters for the myocardial fibers; a_s and b_s are account for the fibers sheet contribution; and a_{fs}, b_{fs} represent the shear effects in the sheet-plane. By considering soft tissue as an incompressible material, the materials parameters will reduce to eight. The finite element method is one of the most reliable approaches for calculating the equilibrium equations when the above model specifies the constitutive model. [16,14]

H.M. Wang et al. [16] are among those who used the Holzapfel et al. framework for developing a three-dimensional computational model of the human left ventricle

myocardium. They considered the myocardium as an inhomogeneous, thick-wall, nonlinearly elastic, and incompressible material. They determined the geometry of the left ventricle by using magnetic resonance imaging. Their research showed that the fiber angle distribution could have a larger impact on the stress inside the left ventricular wall during diastole. However, the sheet orientation had relatively minor effects on stress and stress distribution. They also compared the stress and strain distribution with results obtained from employing other constitutive models and experimental measurements. It was proved that there were large differences in the stress/strain predictions even when the materials parameters were fit to the same experimental data. One of the limitations of the above studies is that they used porcine experimental data to determine the human heart's constitutive model's parameters. They also did not consider the role of initial strains and residual stresses in their model. Finally, in their model, LV was treated as a hyperelastic structure without considering fluid-solid interactions that made the boundary conditions simplified and can alter the resultant stress and strain distributions [16]. H. Gao et al. used the same model. However, they tried to modify it by using a multi-step nonlinear least-squares optimizations procedure to inversely estimate the parameters in the Holzapfel-Ogden constitutive law for myocardium from the pressure-volume and strain data obtained from the LV model. They compared their result with the previous research mentioned here, and they found that the results are close to each other, although some discrepancy was seen in some values along the sheet direction resulting from low sensitivity of the objective functions [14]. Arnab Palit et al. tried to improve the estimation of the myocardium's passive mechanical properties obtained from this method. They introduced a novel method consisting of finite element modeling, response surface method, and genetic algorithm.

They reduced the complexity of the problem by estimating a total of four parameters instead of eight. Their decision was based on the shear responses in six shear modes; From comparing the analytical expression of these six shear modes, it was concluded that only four parameters would be enough to obtain mechanical characteristics of the human myocardium [18]. Although, the uniqueness of the solution cannot be addressed using the above approach in both studies because of the ill-posed nature of the inverse optimization problem and the myocardial properties was extracted by identifying the range of the parameters, instead of the unique value, the response of the material was shown to be robustly determined. Finally, using the above method for modeling the left ventricle, which is so important to model accurately due to its function, had the following limitations: the heterogeneous distribution of the material was not considered in this model, and the in vivo geometry of the left ventricle was reconstructed at early diastole, which was not stress-free, and they needed to consider residual stress which was neglected in the above method. [16,18]

Avazmohammadi et al. [46] took the following approach to address the limitation mentioned in the preceding paragraphs. First, based on a kinematical analysis and using a given strain energy density function (SEDF), they tried to find an optimal set of displacement paths on the full three-dimensional deformation gradient tensor. Then, they applied the obtained data to find novel experimental data from a 1-cm cube of the post-infarcted left ventricular myocardium. In the next step, they developed an inverse finite element of the experimental configuration embedded in a parameter optimization scheme to estimate the SEDF parameters. By this approach, they enhanced the determinability and

predictive capability of the estimated parameters following an optimal design of experiments. Moreover, they could accurately simulate the experimental setup and transmural variation of local fibers directions in the finite element environment. Although there are some limitations regarding their study; The histological measurement of the fiber orientations incorporated into the inverse model did not account for out-of-plane fiber orientation and in-plane variations in the orientations. Also, they only studied the passive behavior of the myocardium, and further investigation needs to be done to predict the behavior of coupled passive-active behavior of the myocardium. [46]

Li et al. [47] have applied a novel three-dimensional numerical-experimental methodology to explore the applicability of an orthotropic constitutive model for passive ventricular myocardium. They tried to integrate three-dimensional optimal loading paths, spatially varying material structure, and inverse modeling techniques. They employed mechanical testing using the triaxial device to apply fully generalized multiaxial deformations on a single cuboidal tissue specimen. They used load cells within minimally restrictive attachment systems to measure the three-dimensional force response of the tissue in real-time. Through the numerical-experimental inverse modeling approach, they tried to extend an existing constitutive model to more fully account for the three-dimensional behavior of the myocardium. This method has led to determining material parameters for healthy myocardium in a cohort of multiple specimens. However, the deformation prescribed in triaxial testing was limited, and it was an approximation of actual deformation undergone by the specimen. They had to introduce a complete constitutive

model to fully capture the full three-dimensional biomechanical response of the left ventricular myocardium. [47]

CHAPTER 3: MODELING METHODOLOGY

Computational reconstruction of the human heart can be divided into four stages: image acquisition, collecting required data, segmentation, and structure reconstruction. The obtained images can be considered a 3D matrix of volume elements, in which the difference in brightness or grayscale distinguishes tissues and structures. Two-dimensional slices contain pixel data; However, a three-dimensional analogy of a pixel where the third dimension is the spatial distance between each slice can be shown by voxel.[2]

Visualizing and reconstructing morphological structures from scanned images obtained from the heart tissue is an active research area. This chapter will discuss the method and process used in this project for image processing and computational modeling.[2]

3.1 Image Acquisition

We used the Images obtained from the previous research done by Shahnaz Javani [5] as a part of her thesis. They used specimens obtained from fresh sheep hearts. {Square specimens were excised from anterior and posterior portions of the left and right ventricle free wall. Samples were cut in a way that the edges were parallel and perpendicular to the predominant direction. Specimens were oriented so that two of the edges were parallel to the main fiber directions. In most samples, one pair of edges was maintained parallel to the

midplane of the atrioventricular valves. Samples were cut with two edges parallel to the most prominent directors of the pectinate muscles visible on the internal surface}.[5]

The obtained specimens from different anatomical regions were used for studying the heart tissue in terms of content and histology. {Ventricular specimens were excised from mid-wall. All the samples were embedded in paraffin and sectioned at a thickness of 4 microns on a microtome. Sections were cut parallel to the endocardial layer. After being put into an oven (approximately 60 degrees C) and cooled, the slides were stained with Masson's trichrome stain. The Masson's trichrome stain rendered myocytes red and collagen fibers blue [5]}. In the next step, we tried to develop a MATLAB code to determine the surface area of each different section, segmentation of each specimen based on its content, and calculation of Young's modulus and Poisson's ratio for each specimen.[5]

3.2 Image segmentation

Segmentation is the process of extracting one or more contiguous regions of interest. More precisely, it is the process of assigning a label to every pixel based on a criterion in an image so that pixels with the same label and that are connected, forming a contiguous region, can be extracted, identified, or categorized. A region within an image can be defined by its pixel properties, boundary, or its interior. Therefore, segmentation approaches can be broadly categorized into the following:

1. Pixel-based: each pixel is labeled based on its grayscale values that represent intensity from the scans.

2. Edge-based: detects edge pixels to form a boundary containing the region of interest.

3. Region-based: considers pixel greyscale levels from neighboring pixels by including similar neighboring pixels.

Pixel-based methods are the simplest and most straightforward approach to implement. However, they lack contextual information and fail in images with high inhomogeneity through a single region. Edge-based methods are the second most straightforward approach, and it is efficient on images of an anatomical structure with clearly defined boundaries, such as the artery. A common problem, however, is that noise or occlusions can cause false or missed edge detection. Region-based methods are the most complex methods since regions of interest include more pixel categorization than edges. This method is helpful in noisy images where edges are difficult to detect. [2,18]

In this project, we used region-based segmentation for partitioning the images into different regions. Color region segmentation is done by defining a set of sample color points representative of a color or range of colors of interest, resulting in an estimate of the 'average' or 'mean' color that we wish to segment. If we consider the average color to be denoted by the image column vector (m). The segmentation objective is to classify each pixel in an image as having a color in the specified range or not. To perform this comparison, we need a measure of similarity. One of the most uncomplicated measures is the Euclidean distance. Let (z) denote an arbitrary point in space. We say that (z) is similar to (m) if the distance between them is less than a specified threshold, T. The Euclidean distance between (z) and (m) is given by:

$$\boldsymbol{D}(z,m) = \|z-m\| = [(z-m)^T(z-m)]^{0.5} = [(z_R - m_R)^2 + (z_G - m_G)^2 + (z_B - m_B)^2]^{0.5} \quad (3.1)$$

Where $\| \, . \, \|$ is the norm of the argument, and the subscripts R, G, and B denote the red, green, and blue components of vectors (m) and (z). The locus of points such that D(z,m)< T is a solid sphere of radius T, as it is illustrated in the following figure (figure a). Points contained within or on the surface of the sphere satisfy the specified color criterion. Coding these two sets of points in the image produces a binary and segmented image. [19,30,31]

A valid generalization of the preceding equation is a distance measure of the form:

$$D(z,m) = [(z-m)^T C^{-1}(z-m)]^{0.5} \quad (3.2)$$

C is the covariance matrix of the samples representative of the color we wish to segment in the above equation. The locus of points such as D(z, m)<T describes a solid, three-dimensional elliptical body with the important property that its principal axes are oriented toward maximum data spread. (figure b). [19,30]

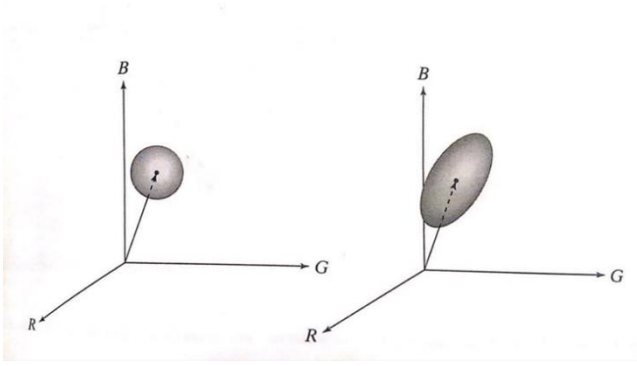

Figure 3.1 Two approaches for enclosing data in RGB vector space for the purpose of segmentation. [19]

We developed the above code in MATLAB for the segmentation of each obtained histological image to three different sections, which are: myocytes (red section), collagen (blue section), and non-collagenous extracellular matrix (ECM) components (yellow part). After dividing each photo into three parts, we transfer the original image to a grayscale image based on the different segments' content. In the next step, we calculate the myocytes and collagen ratio for each segmentation; We transfer the images to a binary image representing collagen as white and the other parts as black; The used code is the same as the previous step; We chose a set of sample color points representing the color related to collagen, which is blue, and we obtained the pixel range related to that color. Then, we transfer those pixels to white and all other pixels to black. Finally, we calculate the white and black parts' surface area, which are equal to collagen and the total area of the images, respectively. We take the same approaches for calculating the area related to other contents.

3.3 Structure Reconstruction

After segmentation of the obtained images, the finite element method is used to analyze the heart tissue's mechanical properties represented in each image. The finite element method is a method for the numerical solution of field problems. A field problem requires that we determine the spatial distribution of one or more dependent variables. [18] Mathematically, a field problem is described by differential equations or by an integral expression. Either description may be used to formulate finite elements. Individual finite elements can be visualized as small pieces of a structure. [18] The word 'finite' distinguishes these pieces from infinitesimal elements used in calculus. A field quantity can have a simple spatial variation in each finite element, perhaps described by polynomial

terms up to X^2, XY, and Y^2. The actual variation in the region spanned by an element is almost certainly more complicated, so finite element analysis provides an approximate solution. Elements are connected at points called nodes. The assemblage of elements is called a finite element structure. The arrangement of elements is called mesh. Numerically, a mesh is represented by a system of algebraic equations to be solved for unknowns at nodes. When combined with the assumed field in any given element, the solution for nodal quantities ultimately determines the field's spatial variation in the element. Although a finite element analysis solution is not exact, the solution can be improved using more elements to represent the structure.[18] The computational procedure for finite element modeling is as follows:

1. Generate matrices that describe element behavior.
2. Connect elements, which implies the assembly of element matrices to obtain a structure matrix.
3. Provide some nodes with loads.
4. Provide other nodes with boundary conditions, which may be called support conditions in structural mechanics.
5. The structure matrix and the array of loads are parts of a system of algebraic equations. Solve these equations to determine nodal values of field quantities.
6. Compute gradients.

In this project, the above steps have been taken to observe the cardiac muscle's behavior under shear and tensile loads and calculate the heart tissue's mechanical properties. In the next section, the mentioned steps will be discussed briefly.[18]

3.3.1 Generate Matrices that Describes Element Behavior

In MATLAB, Each RGB image is defined as a 600 ×800 matrix. The elements represent the pixel values; The pixel range for an RGB image is between zero and 256, demonstrating different colors. We convert the mentioned matrix to a 100 ×100 matrix by averaging the matrices' columns and rows. In the next step, we allocate a specific range of RGB pixel values to each material: collagen, myocytes, and non-collagenous extracellular matrix (ECM) components, based on their color. Extracellular matrix (ECM) components play an essential role in developing and remodeling the cardiovascular systems. The mechanical integrity of the heart tissue relies on the underlying reinforcement of collagen fibers and other extracellular matrix components known as non-collagenous EMC, which are mainly composed of elastin and proteoglycans. They are also important in determining the mechanics of blood vessels, valves, pericardium, and myocardium. [44,45] In this research, we consider the following range for each content:

- 118<pixel<256 for non-collagenous EMC (yellow).
- 0<pixel<100 for myocytes (red).
- 100<pixel<118 for collagen (blue).

We use this range based on the results obtained in the first step to divide each image into three parts based on color. A more detailed description of the used MATLAB code is

discussed in the next chapter. Based on the content, we allocate the different amounts to each element as Young's modulus and Poisson's ratio, which are $E_{Collagen}$= 50 [20], $E_{Myocytes}$=13 [41], and $E_{non\text{-}collagenous\ EMC}$ =24 Kpa [42], $\upsilon_{Collagen}$=0.49 [20], $\upsilon_{Myocytes}$=0.45 [43], and $\upsilon_{non\text{-}collagenous\ EMC}$ =0.48 [44]. The above number was obtained by averaging several studies' experimental data [20,40,21,39,25]. We averaged the obtained results from the previous studies and allocated the above amount to each content. As it can be seen, the Poisson's ratio for all three contents is almost the same since biomaterials are mostly made of water and can be considered incompressible. The collagen fibers behavior was represented by isotropic linear elastic with large displacements to simulate the large strains occurring in the collagen fibers during the ventricles filling. Myocytes is also considered as an isotropic material. However, for more accurate results, the myocytes tissue should be considered a slightly compressible hyperelastic material with relatively soft properties that demonstrate different young's modulus during a cardiac cycle. Furthermore, non-collagenous EMC components should be modeled as a compressible neo-Hookean material instead of isotropic materials. [20,44]

In this project, we assume that the materials' properties are homogenous in each element, enabling us to consider a single value of Young's modulus and Poisson's ratio for each element. The above assumption is accurate when the meshing is refined, eliminating the errors caused by this simplification; The matrices used in this analysis have 10000 elements that represent the original images perfectly and make the above assumption acceptable.

3.3.2 Meshing

For meshing each specimen, we used quadric triangle elements. A quadric triangle is shown in the following figure. It has side nodes in addition to vertex nodes. For stress analysis, the mode degree of freedom is u_i and v_i at each node, i=1, 2…6, for a total of 12 degrees of freedom per element. In terms of the generalized degree of freedom a_i, the element displacement field is the complete quadratic.

$$u=a_1+a_2x+a_3y+a_4x^2+a_5xy+a_6y^2 \tag{3.3}$$

$$v=a_7+a_8x+a_9y+a_{10}x^2+a_{11}xy+a_{12}y^2 \tag{3.4}$$

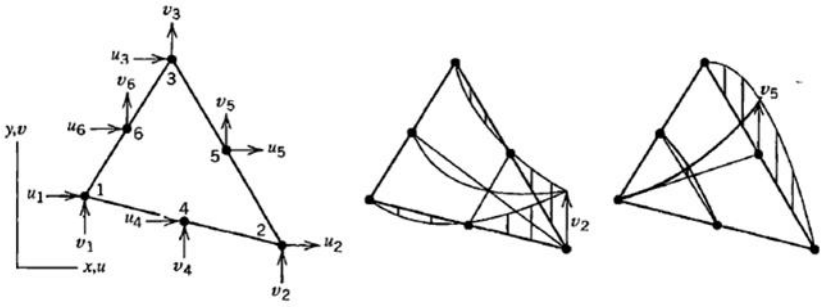

Figure 3.2 (a) Quadric triangle and its 12 nodal d.o.f (b,c) Displacement modes associated with vertex and side d.o.f [18]

element strains are:

$$\varepsilon_x = a_2 + 2a_4x + a_5y \tag{3.5}$$

$$\varepsilon_y = a_9 + a_{11}x + 2a_{12}y \tag{3.6}$$

$$\gamma_{xy} = (a_3 + a_8) + (a_5 + 2a_{10})x + (2a_6 + a_{11})y \tag{3.7}$$

Element strains can vary linearly within the element. Hence the element may be called a 'linear-strain triangle' (LST). Because displacement functions are quadric in x and y, all lines in the element, including its sides, can deform into quadric curves resulting in more accurate results than triangular elements with three nodes. [18] As it was mentioned in the previous section, in this project, 100× 100 matrices were generated, and the final system is as followed:

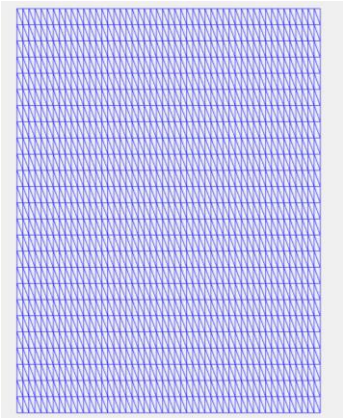

Figure 3.3 The final meshing using for the finite element modeling.

3.3.3 Boundary condition and Loads

We applied three different forces to the designed matrices. The applied forces are as follow:

- Tensile stress in Y direction: We applied concentrated forces to the nodes located on the top and bottom sides in the Y direction.
- Tensile stress in X direction: We applied concentrated forces to the nodes located on the left and right sides in the X-direction.

- Shear stress: We apply concentrated forces to the nodes located on the top and bottom sides in the x-direction and the nodes located on the right and left sides in the y-direction.

The applied forces are equal to 0.4 N, which is equal to the force that is experienced by the ventricles [39]. We found the mentioned amount from the previous study done by Arvidsson et al. [39]; They tried to quantify three-dimensional hemodynamics forces in both ventricles using magnetic resonance imaging four-dimensional flow measurement. [39] They used four-dimensional flow data as input for the Navier-Stokes equation to compute hemodynamics forces over the entire cycle. [39]. They divided the left and right ventricles into three parts and calculated the applied forces on each part during a cardiac

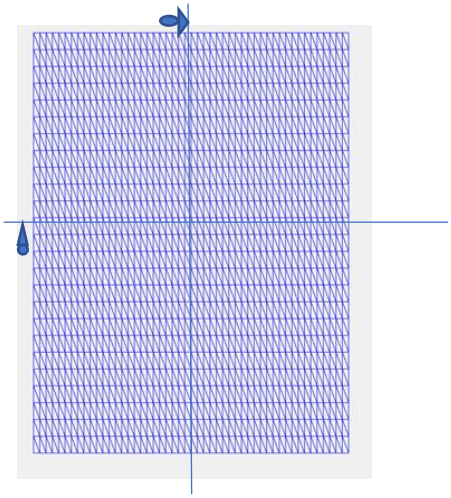

Figure 3.4 boundary conditions using for the finite element modeling.

cycle. We took an average from the obtained forces through the ventricles and used the result in this project. In this simulation, we applied uniform and concentrated forces to the nodes located on the sides of the specimen. We applied half of the applied force to the nodes located on the edges that joined two sides of the specimen for obtaining more accurate results. Then, we specify the boundary conditions; We assume that the horizontal

symmetric line is fixed in the y-direction and the vertical symmetric line is fixed in the x-direction, which means there is no displacement and rotation in those directions. The following figure demonstrates the mentioned boundary conditions.

3.3.4 Formulation techniques

In a finite element analysis, shape functions are used to interpolate both displacement fields and element geometry. Displacement of a point within an element can be expressed in terms of the nodal Degree of freedom {d} and shape functions [N], which are functions of reference coordinate. Similarly, the global position of a point within the global coordinate of a point within the element can be expressed in terms of global nodal positions and shape functions $[\widetilde{N}]$ which are also functions of reference coordinates. [18]

Generally,

- Nodal degree of freedom {d} define displacement [u v w] of a point within the element which is equal to: $[u\ v\ w]^T = [N]\{d\}$.
- Nodal coordinates {c} define coordinates [x y z] of a point within the element which is equal to: $[x\ y\ x]^T = [\widetilde{N}]\{c\}$.

As mentioned earlier, the shape function matrices are functions of reference coordinates: r, s, and t. They are attached to the element and maintain their position with respect to it, regardless of the element's global coordinate. Also, an element's physical size and shape have no effect on the numerical values of reference coordinates at which nodes appear. Thus, physical elements of various sizes and shapes are all mapped into the same size and shape in reference coordinates. For the stress analysis problems, the three-node

triangles and four-node tetrahedrons are susceptible to shear locking behavior. So, higher-order elements, the six-node triangular, are preferred choices. That is why we chose six-node triangular elements in this study. [18]

If side and internal nodes have a regular pattern, one can generate triangular elements containing a complete polynomial in Cartesian coordinate. Mapping the triangular elements into reference coordinate rs, the six-node triangle has nodes at the exact location, regardless of the physical element's shape and size. [18] For the six-node triangular elements, each shape function is the product of functions called line functions, which are:

$$N_1 = (1-r-s)\times(1-2r-2s) \quad N_2 = r\times(2r-1) \quad N_3 = s\times(2s-1)$$

$$N_4 = 4r\times(1-r-s) \qquad N_5 = 4rs \qquad N_6 = 4s\times(1-r-s) \qquad (3.8)$$

Because the element is isoperimetric, the same shape functions are used to interpolate both coordinate and displacement of a point within the element from coordinates and displacement of nodes. Thus,

$$\begin{Bmatrix} x \\ y \end{Bmatrix} = \begin{bmatrix} \sum N_i x_i \\ \sum N_i y_i \end{bmatrix} = [N]\{c\} \qquad \begin{Bmatrix} u \\ v \end{Bmatrix} = \begin{bmatrix} \sum N_i u_i \\ \sum N_i v_i \end{bmatrix} = [N]\{d\} \qquad (3.9)$$

Where index (i) in summation runs from 1 to 6, and,

$$\{c\} = [x_1\ y_1\ x_2\ y_2\ x_3\ y_3\ x_4\ y_4\ x_5\ y_5\ x_6\ y_6]^T \qquad (3.10)$$

$$\{d\} = [u_1\ v_1\ u_2\ v_2\ u_3\ v_3\ u_4\ v_4\ u_5\ v_5\ u_6\ v_6]^T \qquad (3.11)$$

$$[N] = \begin{bmatrix} N_1 & 0 & N_2 & 0 & N_3 & 0 & N_4 & 0 & N_5 & 0 & N_6 & 0 \\ 0 & N_1 & 0 & N_2 & 0 & N_3 & 0 & N_4 & 0 & N_5 & 0 & N_6 \end{bmatrix} \qquad (3.12)$$

And {d} lists the nodal displacement (d.o.f) of an element. Strain is determined from displacement from $\{\varepsilon\} = [\partial]\{u\}$. Hence:

$$\{\varepsilon\} = [B]\{d\} \quad where \ [B] = \{\partial\}[N] \tag{3.13}$$

Matrix [B] is called the strain-displacement matrix. [B] cannot be written as quickly as the equations discussed above because it involves gradients and derivations, which cannot be easily calculated. So, we consider a function $\varphi(r, s)$ and examine its derivation with respect to x and y. Here (φ) may represent u or v. Derivatives with respect to x and y are not available directly, and they can be obtained by using the derivatives with respect to r and s. [18]

$$\frac{\partial \varphi}{\partial r} = \frac{\partial \varphi}{\partial x}\frac{\partial x}{\partial r} + \frac{\partial \varphi}{\partial y}\frac{\partial y}{\partial r} \tag{3.14}$$

$$\frac{\partial \varphi}{\partial s} = \frac{\partial \varphi}{\partial x}\frac{\partial x}{\partial s} + \frac{\partial \varphi}{\partial y}\frac{\partial y}{\partial s} \tag{3.15}$$

Or

$$\begin{Bmatrix} \varphi_{,r} \\ \varphi_{,s} \end{Bmatrix} = [J] \begin{Bmatrix} \varphi_{,x} \\ \varphi_{,y} \end{Bmatrix} \tag{3.16}$$

Where [J] is called the Jacobian matrix.

Using the above equations, we can obtain the following equation for the calculation of the strain-displacement matrix:

$$[B] = \begin{Bmatrix} \frac{\partial}{\partial x} & 0 \\ 0 & \frac{\partial}{\partial y} \\ \frac{\partial}{\partial y} & \frac{\partial}{\partial x} \end{Bmatrix} \begin{bmatrix} N_1 & 0 & N_2 & 0 & N_3 & 0 & N_4 & 0 & N_5 & 0 & N_6 & 0 \\ 0 & N_1 & 0 & N_2 & 0 & N_3 & 0 & N_4 & 0 & N_5 & 0 & N_6 \end{bmatrix} \quad (3.17)$$

Stress-strain relation can be written as:

$$\{\sigma\} = [C]\{\varepsilon\} + [\sigma_0] \quad (3.18)$$

Subscript zero indicates initial values. The constitutive matrix [C] is the elastic constant for each element. [C] is symmetric and can represent isotropic or anisotropic material properties. For isotropic element and plane stress condition, the above equation can be written for a two-dimensional system as:

$$\begin{Bmatrix} \sigma_x \\ \sigma_y \\ \tau_{xy} \end{Bmatrix} = [C] \times \begin{Bmatrix} \varepsilon_x \\ \varepsilon_y \\ \gamma_{xy} \end{Bmatrix} \qquad [C] = \frac{E}{(1-\vartheta^2)} \begin{bmatrix} 1 & \vartheta & 0 \\ \vartheta & 1 & 0 \\ 0 & 0 & 0.5(1-\vartheta) \end{bmatrix} \quad (3.19)$$

$$\begin{bmatrix} \varepsilon_x \\ \varepsilon_y \\ \varepsilon_{xy} \end{bmatrix} = \begin{bmatrix} \frac{\delta}{\delta x} & 0 \\ 0 & \frac{\delta}{\delta y} \\ \frac{\delta}{\delta x} & \frac{\delta}{\delta y} \end{bmatrix} \begin{bmatrix} u \\ v \end{bmatrix} \; or \; [\varepsilon] = [B]\{d\} \quad (3.20)$$

We can obtain the following equation by using stress-strain relation and the above equations:

$$(\partial d)^T (\int [B]^T [E][B] dV\{d\} - \int [B]^T [E](\varepsilon_0) dV + \int [B]^T \{\sigma_0\} dV - \int [N]^T \{F\} dV - \int [N]^T \{\varphi\} ds) = 0 \quad (3.21)$$

Vector {d} and {∂d} do not appear within integral because they are not a coordinate function. Therefore, the above equation yields,

$$[K]\{d\} = \{F\} \tag{3.22}$$

{F} is the vector of loads applied to structure nodes by elements due to all sources, and [K] is the global stiffness matrix.

Moreover, the element stiffness matrix is:

$$[k] = \int [B]^T [C][B] dv \tag{3.23}$$

In this project, the mentioned equations were used to develop a MATLAB code, which enabled us to calculate each image's stress and strain matrices. For this aim, we consider different [C] matrix for which element based on the content (collagen, non-collagenous EMC, and myocytes) as we allocate specific Young's Modulus and Poisson's ratio to each content; Then, the elemental and global stiffness matrices were calculated from the defined [C] and [B] matrices using the above formulations. Finally, stress and strain matrices were calculated using the defined loads and boundary conditions.

3.4 Calculation of the Global modulus

For the calculation of the global Young's modulus in the x and y direction and the shear modulus, we used the following approaches:

- Calculation of the global Young's modulus in x-direction: In the first step, the tensile force was applied to the right and left sides in the x-direction. Then, we calculate the total displacement on the mentioned sides using the finite element method. For this aim, we sum the total displacement of the right and left sides in the x-direction and divide it by the number of nodes on those sides to calculate the

average displacement. We calculate the average stress by dividing the total applied force in the x-direction by the area in the next step. Finally, we obtained the average stain, stress, and the global Young's modulus in the x-direction, utilizing the following equations:

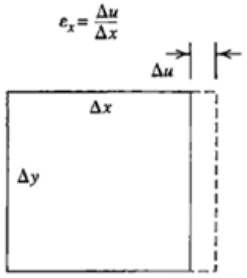

Figure 3.5 An infinitesimal rectangle, subjected to x-direction normal strain [18]

$$\Delta u, \Delta v = \frac{avaerage\ nodal\ dospalcement}{number\ of\ the\ nodes\ on\ the\ \ side} \tag{3.24}$$

$$\overline{\varepsilon_x} = \frac{\Delta u}{\Delta x} \qquad \overline{\sigma_x} = \frac{\sum F_X}{A} \tag{3.25}$$

$$\overline{E_x} = \frac{\overline{\sigma_x}}{\overline{\varepsilon_x}} \tag{3.26}$$

- Calculation of the global Young's modulus in y-direction: In the first step, the tensile force was applied to the top and bottom sides in the y-direction. Then, we calculate the total displacement on the mentioned sides using the finite element method. For this aim, we sum the total displacement of the top and bottom sides in the y-direction and divide it by the number of nodes on those sides to calculate the average displacement. We calculate the average stress by dividing the total applied force in the y-direction by the area in the next step. Finally, we obtained the average

stain, stress, and the global Young's modulus in the y-direction, utilizing the following equations:

$$\overline{\varepsilon_y} = \frac{\Delta v}{\Delta y} \quad \overline{\sigma_y} = \frac{\sum F_y}{A} \tag{3.27}$$

$$\overline{E_y} = \frac{\overline{\sigma_y}}{\overline{\varepsilon_y}} \tag{3.28}$$

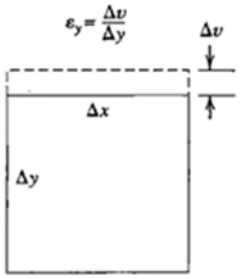

Figure 3.6 An infinitesimal rectangle, subjected to y-direction normal strain [18]

- Calculation of the global shear modulus: In the first step, the shear force was applied in the x-direction on the top and bottom sides and in the y-direction on the right and left sides. Then, we calculate the total displacement on the left side and the bottom sides in the x and y-direction, respectively. Finally, we obtained the average stain, stress, and the global shear modulus, utilizing the following equations:

$$\overline{\varepsilon_{xy}} = \frac{\Delta v}{\Delta x} + \frac{\Delta u}{\Delta y} \quad \overline{\tau_{xy}} = \frac{\sum F_{xy}}{A} \tag{3.29}$$

$$\overline{E_{xy}} = \frac{\overline{\tau_{xy}}}{\overline{\varepsilon_{xy}}} \tag{3.30}$$

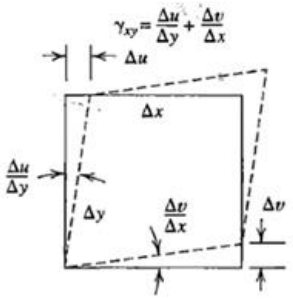

Figure 3.7 An infinitesimal rectangle, subjected to shear strain [18]

CHAPTER 4: RESULTS

This thesis aimed to describe the heart tissue's mechanical properties and develop computational models to identify the cardiac tissue's behavior under different stress/strain conditions. A set of images obtained from left and right ventricles were used for developing a comprehensive model for the simulation of the ventricles. Finite element methods were employed to predict the displacement, stress, and strain of the heart tissue under the applied force of 0.4 N under three different loading conditions: normal force in the x-direction, normal force in the y-direction, and shear force. This force is equal to the force that is experienced by the ventricles. [39] Computational methods simulated the mechanical behavior of the heart muscle under tensile and shear stress; The obtained results can be used to calculate the heart tissue's global behavior, and this quantification can reveal how this behavior influences the heart's performance. In this chapter, the obtained results will be discussed and compared with previous studies.

4.1 Image Processing

As mentioned in the previous chapter, we did the histological analysis on the images obtained from the left and right ventricles by Shahnaz Javani [5]. She used Masson's trichrome for staining the images, which effectively rendered myocytes red, non-collagenous EMC yellow, and collagen fibers blue. [5] Myofibers arranged themselves in a parallel orientation in the ventricles, and changes in fiber direction are almost very

smooth. The collagen fibers play an essential role in the cardiac tissue's mechanical properties, which are primarily found as collagen I and collagen III; however, collagen I is much stiffer than collagen III and, as such, is the primary controller of myocardial tissue properties under deformation. [32]. Collagen I is a relatively stiff protein with a highly nonlinear stress-strain profile. Collagen provides little resistance at low amounts of a stretch but large amounts of resistance at a large stretch. The collagen's primary purpose in the healthy myocardium is to prevent overstretch and provide a surface for the myocytes to attach to in order to aid in the transmission of contractile force to the tissue. In healthy tissues, the amount of collagen is meager, but it can become elevated due to disease or aging through a process known as fibrosis. [33,34,35,36]. An excess of collagen fibers increases the tissue's stiffness, which reduces the ventricles' ability to fill with blood. [37,38] Previous studies show that collagen fibers in the ventricles contribute to tensile stiffness, especially at higher cavity volumes, while maintaining myocytes' architecture, myofiber bundles, and sheets. Large, coiled perimysium collagen fibers provide tensile stiffness, whereas smaller endomysia fibers surrounding and interconnecting individual myocytes are thought to prevent myocyte slippage and maintain unloaded ventricular geometry. In this project, we tried to find a correlation between collagen variation and the left and right ventricles' mechanical properties.

For analyzing the compositions of the samples, a MATLAB code was developed. In the first step, we tried to divide each image into three different regions based on the content using the region-based segmentation method discussed in the previous chapter. For this aim, we defined a set of sample points representative of a color or range of colors of

interest, resulting in an estimate of the 'average' or 'mean' color that we wish to segment. These ranges can be considered a sphere, and any points contained within or on the surface of this sphere satisfy the specified color criterion. In other words, we classify each pixel in the images as having a color in the specified range or not. For this comparison, the obtained criteria for each color is: 118<pixel<256 for non-collagenous EMC (yellow), 0<pixel<100 for myocytes (red), and 100<pixel<118 for collagen (blue). After dividing each image into three parts, we transfer the images to grayscale images; A grayscale image is a data matrix whose values represent one image pixel's intensities. Using the obtained results, we developed a MATLAB code to transfer each image to a grayscale image based on its intensity. Through this code, we transferred the segmented images obtained in the previous steps to grayscale images. In the final images, collagen, non-collagenous EMC, and myocytes are represented by white, black, and gray. The developed MATLAB codes are attached to the appendix for future information.

The results of the image processing are shown in the following figure. In the following figure, we showed the original images and the obtained grayscale images; The first three images were obtained from the left ventricle. The rest three images were obtained from the right ventricle. The grayscale images presented collagen, non-collagenous EMC, and myocytes by white, black, and gray. [11,5].

In the next step, we used the above results for the calculation of the collagen surface ratio. We calculated each content's total surface area by transferring each photo to a binary image. For this aim, we used the same range mentioned in the previous step and demonstrate the desired content and color as white and all other contents as black. Then,

we calculate the surface area associated with the white part. We repeated the same process for each content. The final results will be discussed in the next section.

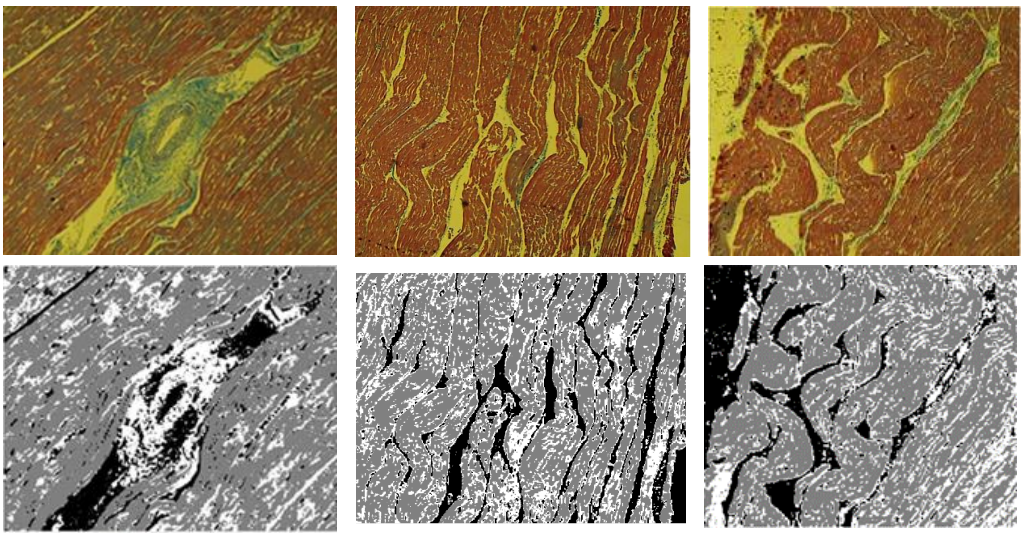

Figure 4.1 the segmentation results from the images obtained from left ventricle. The collagen, non-collagenous EMC, and myocytes show by white, black and gray

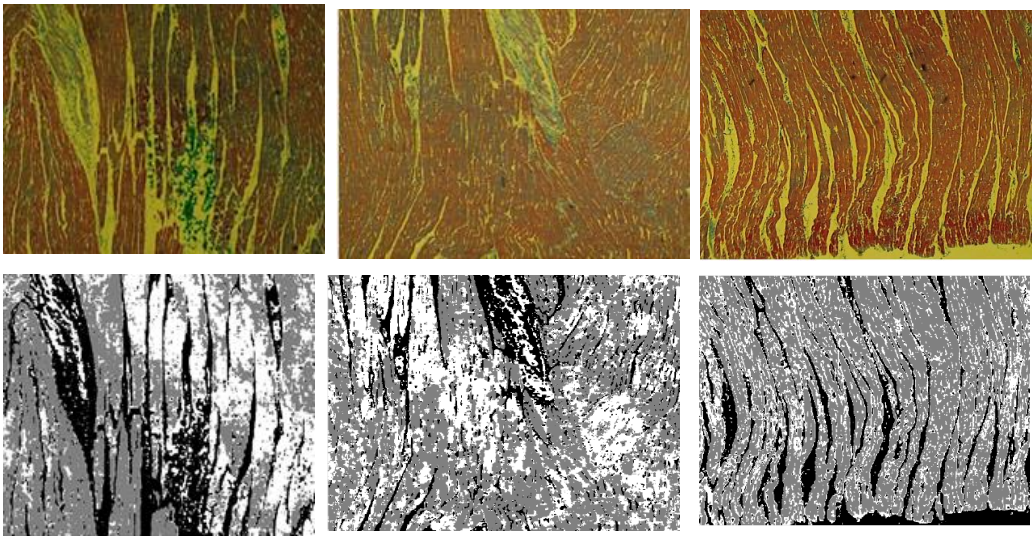

Figure 4.2 the segmentation results from the images obtained from right ventricle. The collagen, non-collagenous EMC, and myocytes show by white, black and gray

The average surface area ratio of collagen and collagen to myocytes was calculated for each image, and the results were summarized in the following table. A collagen network, mainly composed of type I and III fibrillar collagen, is found in the myocardium's extraocular space. [32] This network has multiple functions, including preserving tissue architecture and chamber geometry, assisting in the enlengthening of myocytes, providing tensile strength to myocytes to prevent rapture, and preventing cardiac myocytes slippage. [32] Collagen is a major determinant of tissue stiffness, and the architecture and stiffness of the myocardium and the geometry of its ventricular chambers would falter without fibrillar collagen. Based on obtained results in this study, The average amount of collagen is almost the same in the left and right, with an average amount of 0.1968 for collagen ratio and 0.3171 for collagen to myocytes ratio. However, the collagen content is slightly higher in the left ventricle, which explains the underlying fact that the left ventricle has to be more substantial compared to the right ventricle because of its function, which is to pump oxygen-rich blood to the rest of the body through the aortic valve; So, it must function effectively under higher pressure and residual stress. We examined a small number of samples since we have difficulty accessing more samples from the previous study. For a more precise and accurate evaluation of the correlation between the cardiac tissue's microstructure and passive mechanical properties, we need to examine more samples and investigate further.

Table 4.1. calculation of the collagen content

Image's number	Collagen Ratio	Collagen/myocytes Ratio
1 (LV)	0.2452	0.3996
2 (LV)	0.1921	0.2761
3 (LV)	0.2180	0.3860
4 (RV)	0.1156	0.1443
5 (RV)	0.2141	0.3655
6 (RV)	0.1962	0.331
Mean	0.1968	0.3171
Standard Derivation	0.0441	0.0955

4.2 Stress-Strain analysis

In this step, we used the image segmentation process results and transferred each image to a matrix. We convert each matrix representing the images to a 100 ×100 matrix by averaging the matrices' columns and rows. A certain amount of Young's modulus and Poisson's ratio were allocated to each matrix's element based on their content: collagen, non-collagenous EMC, and myocytes, which are $E_{Collagen}$= 50 [20], $E_{Myocytes}$=13 [41], and $E_{non\text{-}collagenous\ EMC}$ = 24 Kpa [42], $\upsilon_{Collagen}$=0.49 [20], $\upsilon_{Myocytes}$=0.45 [43], and $\upsilon_{non\text{-}collagenous\ EMC}$=0.48 [44]. For this aim, we used the same pixel range that we used for the image segmentation in the previous section for defining the different content. The defined criteria

for each color are: 118<pixel<256 for non-collagenous EMC(yellow), 0<pixel<100 for myocytes (red), and 100<pixel<118 for collagen (blue). the results are shown in the following images: In the following images, Young's modulus present for collagen, non-collagenous EMC, and myocytes by yellow, light blue, and dark blue, and the Poisson's ratio present for collagen, non-collagenous EMC, and myocytes by yellow, dark yellow, and dark blue. In the following figures, matrices related to two samples from the left and right ventricles are demonstrated. More results showing matrices related to the remaining samples are attached to the appendix.

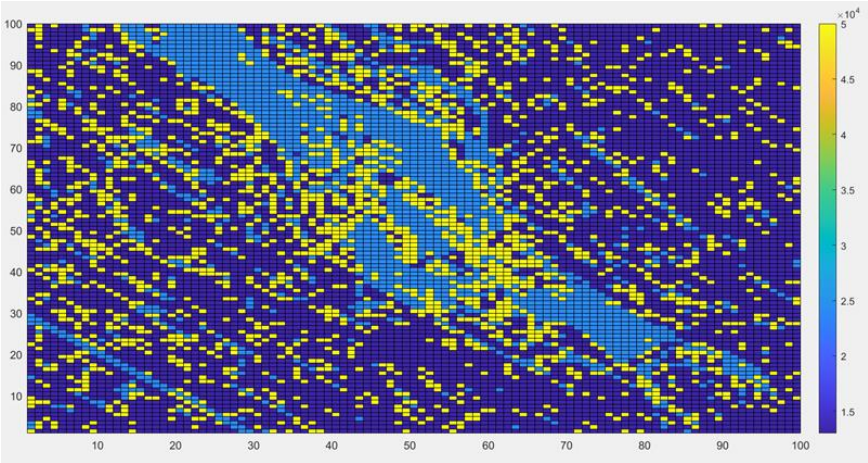

Figure 4.3 The Young's modulus matrix related to a sample obtained from the left ventricle.

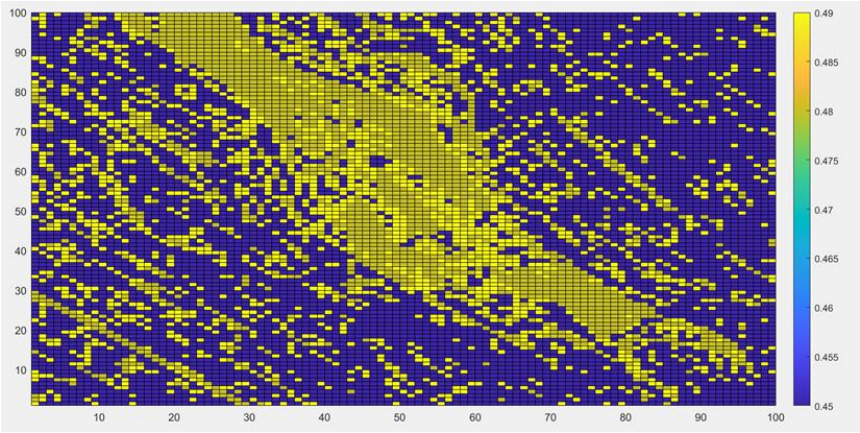

Figure 4.4 Poisson's ratio matrix related to a sample obtained from the left ventricle.

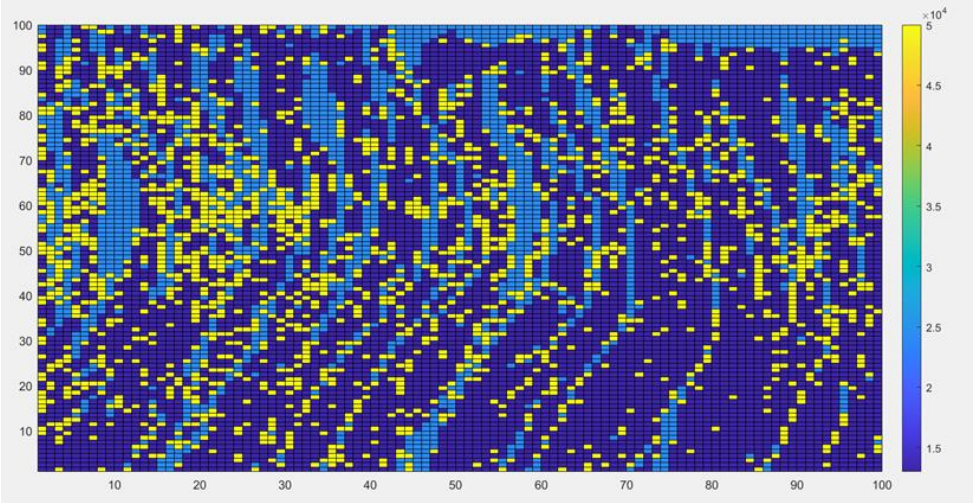

Figure 4.5 The Young's modulus matrix related to a sample obtained from the right ventricle.

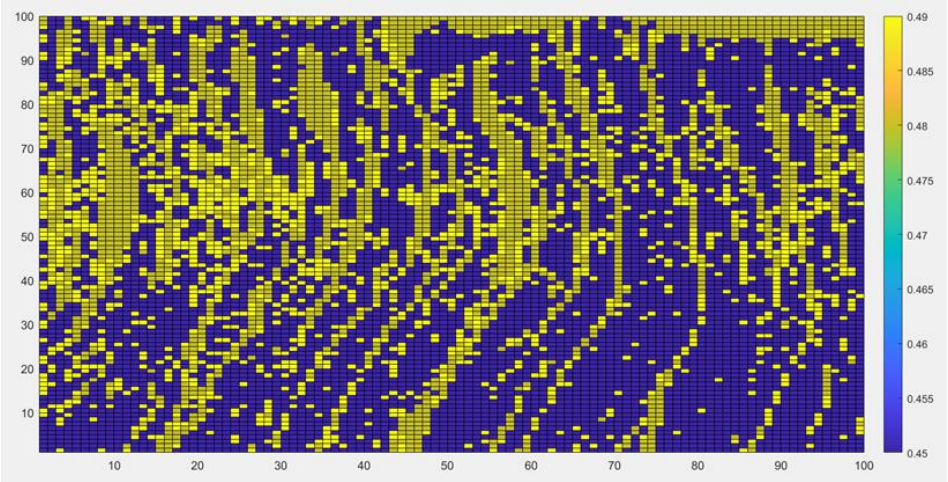

Figure 4.6The Poisson's ratio matrix related to a sample obtained from the right ventricle.

In the next step, the forces were applied. The blood flow is driven by hemodynamic forces that are exchanged between the blood and the myocardium. LV forces were mainly aligned along the apical-basal longitudinal axis, with an additional component aimed toward the aortic valve during systole. Conversely, RV forces were found in both longitudinal and short-axis planes. [39] Previous studies showed that all regions

demonstrated a nonlinear response to applied forces. However, the left and right ventricles have less pronounced nonlinearity than other regions of the heart.

Furthermore, the left and right ventricles' stress-strain curves had a greater slope in the main fiber direction than the cross-fiber direction as the tissue was significantly stiffer in the fiber direction than the cross-fiber direction. [5] We applied tensile force in the x and y direction and shear force to observe the cardiac tissue behavior in different stress/strain conditions. In the following section, we will discuss the obtained results in more detail.

4.2.1 Tensile Stress in Y-direction

This study developed a MATLAB code using finite element analysis to calculate the heart's mechanical properties. In the first step, we defined the boundary conditions and fixed the horizontal symmetric lines in the y-direction and the vertical line in the x-direction. Then, the tensile force of 0.4 N was applied to the top and bottom sides in the y-direction. This force is equal to the average force that the ventricles undergo during a cardiac cycle. [39] Finally, we calculated the total displacement on the mentioned sides in the y-direction using finite element analysis. The obtained results are shown in the following figures: The first figure is for the left ventricle, and the second image is obtained from the right ventricle; As was expected, the deformation is not homogenous in the ventricles, although it is more considerable in the left ventricle. The underlying fact causing this is that cardiac tissue is categorized as a heterogeneous, anisotropic, nonlinear soft tissue that undergoes large deformation. Also, we considered that the heart tissue comprises three different materials with various properties, which results in various behavior under the same loading condition. Furthermore, the other point that must be considered is that the

right ventricle demonstrated more considerable deformation explaining that it has a lower young's modulus and is less stiff. The results agree with the obtained results from microstructure analysis done earlier, which showed that the right ventricle has a lower collagen ratio than the left ventricle. The following figures demonstrated the initial and deformed structures of two samples from the left and right ventricles. More figures can be found in the appendix.

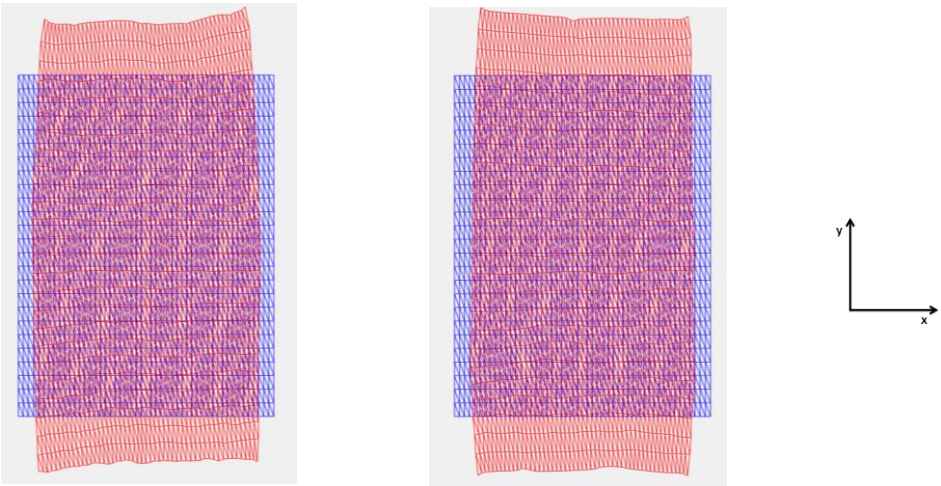

(a) (b)

Figure 4.7 The original and deformed structure of the (a) left ventricle (b) right ventricle samples under tensile stress in y-direction.

4.2.2 Tensile Stress in X-direction

We took the same approach for the calculation of the tensile stress in the x-direction. In the first step, we defined the boundary conditions and fixed the horizontal symmetric lines in the y-direction and the vertical line in the x-direction. Then, the tensile force of 0.4 N was applied to the right and left sides in the y-direction. Finally, we calculated the total displacement on the mentioned sides. The obtained results are shown in the following figures: The first figure is for the left ventricle, and the second image is

obtained from the right ventricle; The results show that both ventricles demonstrated inhomogeneous deformation the same as the previous loading condition. Also, the right ventricles have higher displacement than the left ventricles resulting from the fact that the left ventricle has a higher young's modulus than the right ventricle. Comparing the results related to the tensile loading in the y-direction with the loading in the x-direction; We can see that the displacement is more considerable in the y-direction caused by the underlying fact that the samples demonstrated higher stiffness in the X-direction.

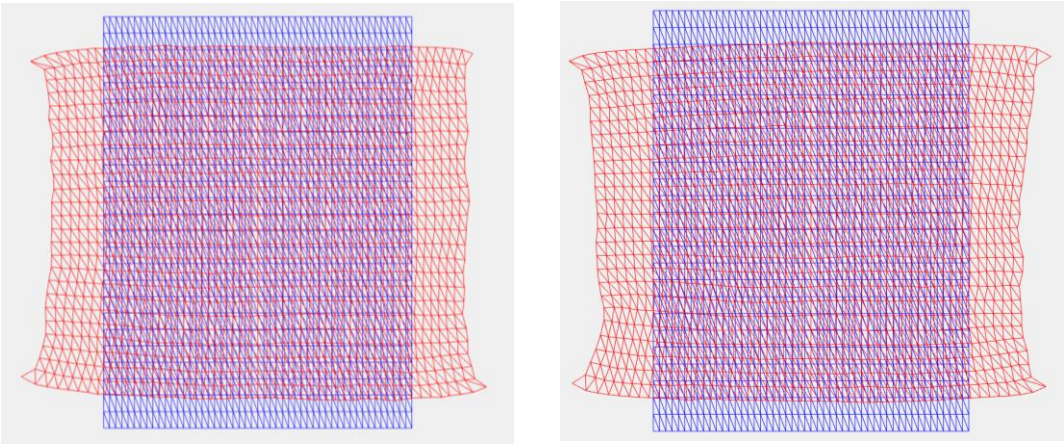

(a) (b)

Figure 4.8 The original and deformed structure of the (a) left ventricle (b) right ventricle samples under tensile stress in x-direction.

4.2.3 Shear Stress

We took the same approach for the calculation of the shear stress. In the first step, we defined the boundary conditions and fixed the horizontal symmetric lines in the y-direction and the vertical line in the x-direction. Then, the shear force of 0.4 N was applied to the right and left sides in the y-direction and to the top and bottom sides in the x-direction. Finally, we calculated the total displacement on the mentioned sides using the

previous chapter's equations. The obtained results are shown in the following figures: The first figure is for the left ventricle and the second image obtained from the right ventricle; The displacement is considerably lower than the tensile loading conditions caused by the underlying fact that the ventricles have low shear stiffness. The deformation is not homogenous because the cardiac tissue's mechanical properties are anisotropic, nonlinear, and inhomogeneous. Moreover, the deformation is almost the same in the right and left ventricle, and it shows minor variation, unlike the tensile loading conditions, which produced higher displacement in the right ventricle. Based on the points mentioned above, it was concluded that the shear loading is more complicated than the tensile loading conditions caused by the fact that forces were applied on all sides producing deformation in both x and y-direction. So, we need to develop a more sophisticated model to evaluate the response of the cardiac tissue under shear loading more accurately.

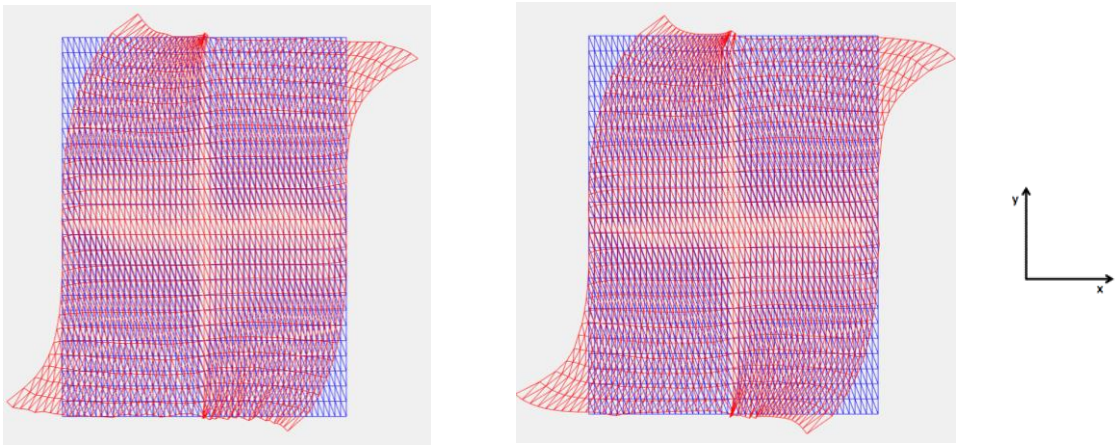

(a) (b)

Figure 4.9 The original and deformed structure of the (a) left ventricle (b) right ventricle samples under shear stress.

We calculate the average Young's modulus in the x and y direction and shear modulus from the above data, including the displacement, stress, and strain. For this aim, we calculated the average displacement on the sides and divided them by the specimen's length to obtain the average strain. Then, we calculated the average stress by dividing the total force by area. A more detailed description of the procedure was discussed in the previous chapter. The obtained results are as followed. The Young's modulus is almost the same in the x and y direction; however, as expected, the obtained average Young's modulus is more significant in the x-direction than the y-direction as the specimens showed lower displacement in the x-direction. The shear stiffness is much lower than Young's modulus and has an average of 11.6 KPa. Moreover, the amount of the shear stiffness is almost the same in the samples obtained from the left and right ventricles. Although, it is more considerable in the left ventricle. The obtained results have a good agreement with the previous studies making the used method reliable to be used in future studies. However, more research must be developed by using a three-dimensional model. Also, we have to consider the heterogeneous behavior of the contests, especially myocytes, to obtain more accurate results.

Table 4.2. Calculation of the moduli

Image Number	**Young's Modulus in y Direction**	**Young's Modulus in x Direction**	**Shear Modulus**
1 (LV)	88 KPa	153 KPa	13 KPa
2 (LV)	85 KPa	146 KPa	11 KPa
3 (LV)	86 KPa	150 KPa	13 KPa
4 (RV)	72 KPa	133 KPa	9 KPa
5 (RV)	86 KPa	148 KPa	12 KPa
6 (RV)	84 KPa	148 KPa	12 KPa
Mean	83.5 KPa	146.33 KPa	11.6 KPa
Standard Derivation	5.78	6.95	1.51

In this section, we tried to find the mechanical properties of the specimens along the fibers and in the cross-fiber direction. The obtained results provide valuable information about the behavior of the heart tissue, and we can study the effects of the fibers' orientation on the global behavior of the tissues. We calculated the myocytes fibers' direction from the original images of the left and right ventricles for this aim. Based on the obtained images, the myocytes' fibers are oriented more horizontally. We used the

following equations for obtaining the strain and stress values in the fibers' direction from the previously calculated values in the X and Y-direction:

$$\begin{bmatrix} \varepsilon_1 \\ \varepsilon_2 \\ \varepsilon_{12} \end{bmatrix} = [T] \begin{bmatrix} \varepsilon_x \\ \varepsilon_y \\ \varepsilon_{xy} \end{bmatrix} \tag{5.1}$$

Where,

$$[T] = \begin{bmatrix} c^2 & s^2 & 2cs \\ s^2 & c^2 & -2cs \\ -cs & cs & c^2 - s^2 \end{bmatrix} \tag{5.2}$$

However, to work in terms of engineering strains, using $\gamma_{xy} = 2\varepsilon_{xy}$, then [T] must be modified and changed to:

$$[T'] = \begin{bmatrix} c^2 & s^2 & cs \\ s^2 & c^2 & -cs \\ -2cs & 2cs & c^2 - s^2 \end{bmatrix} \tag{5.3}$$

In which c=cos(ϕ) and s=sin(ϕ). The same matrix can be used to transform tensorial stresses so that,

$$\begin{bmatrix} \sigma_1 \\ \sigma_2 \\ \tau_{12} \end{bmatrix} = [T] \begin{bmatrix} \sigma_x \\ \sigma_y \\ \tau_{xy} \end{bmatrix} \tag{5.4}$$

As expected, the samples demonstrated higher mechanical properties along the fibers than the cross-fiber direction. The mean value for Young's modulus was calculated as 235.33 and 185. 83 KPa along fibers and in the cross-fiber direction. The calculated shear stiffness is also higher through the fiber's direction than the X and Y direction, with an average of 40.16 Kpa. The obtained results are shown in the below table.

Table 4.3. Calculation of the moduli

Image Number	Young's Modulus along fibers	Young's Modulus in cross-fiber direction	Shear stiffness
1 (LV)	261 KPa	210 KPa	54 KPa
2 (LV)	246 KPa	191 KPa	41 KPa
3 (LV)	240 KPa	190 KPa	39 KPa
4 (RV)	234 KPa	187 KPa	38 KPa
5 (RV)	227 KPa	175 KPa	36 KPa
6 (RV)	204 KPa	162 KPa	33 KPa
Mean	235.33 KPa	185.83 KPa	40.16
Standard Derivation	19.22	16.22	7.31

4.3 Calculation of the Compliance Matrix

In this step, we tried to calculate the compliance matrix related to each sample. Compliance matrix is a symmetric matrix that related the strain matrix to the stress matrix by the following equations:

$$\{\varepsilon\} = [S]\{\sigma\} \tag{5.5}$$

Where [S] is a compliance matrix and can be calculated as:

$$[S] = \begin{bmatrix} 1/E_x & -\vartheta_{xy}/E_x & 0 \\ -\vartheta_{yx}/E_y & 1/E_y & 0 \\ 0 & 0 & 1/G_{xy} \end{bmatrix} \tag{5.6}$$

In the above equations, E_x, E_y, $\nu_{xy/yx}$, and G_{xy} represent Young's modulus in the x and y direction, Poisson's ratio, and shear stiffness, respectively. For calculating the Poisson's ratio, we calculate the strain in the x and y direction when we applied tensile loading in the previous step. Then, we used the following equation for the calculation of Poisson's ratio.

$$\vartheta_{xy} = -\frac{Strain\ in\ the\ direction\ of\ the\ load}{Strain\ at\ the\ right\ angle\ of\ the\ load} = -\frac{\varepsilon_x}{\varepsilon_y} \tag{5.7}$$

$$\vartheta_{yx} = -\frac{Strain\ in\ the\ direction\ of\ the\ load}{Strain\ at\ the\ right\ angle\ of\ the\ load} = -\frac{\varepsilon_y}{\varepsilon_x} \tag{5.8}$$

The obtained results are shown in the below table.

Table 4.4. calculation of the Poisson's Ratio

Image Number	ϑ_{yx}	ϑ_{xy}
1 (LV)	0.4	0.41
2 (LV)	0.46	0.36
3 (LV)	0.36	0.43
4 (RV)	0.42	0.36
5 (RV)	0.45	0.4
6 (RV)	0.43	0.45
Mean	0.42	0.41
Standard Derivation	0.0363	0.0365

As expected, the obtained results are in the range of 0.4, demonstrating the underlying fact that the cardiac tissue can be considered almost incompressible. The obtained results were used for the calculation of the constitutive matrix elements. The following table shows the final results.

Table 4.5 Calculation of the compliance matrix

Image	**S_{11}**	**S_{22}**	**S_{33}**	**S_{12}**	**S_{21}**
1 (LV)	0.006536	0.011364	0.076923	-0.00268	-0.00455
2 (LV)	0.006849	0.011765	0.090909	-0.00247	-0.00541
3 (LV)	0.006667	0.011628	0.076923	-0.00287	-0.00419
4 (RV)	0.007519	0.013889	0.1111	-0.00271	-0.00583
5 (RV)	0.006757	0.011628	0.08333	-0.0027	-0.00523
6 (RV)	0.006757	0.011905	0.08333	-0.0027	-0.00512
Mean	0.006847	0.01203	0.0871	-0.00274	-0.00505
Standard Derivation	0.000346	0.000928	0.012857	0.000194	0.000597

4.4 Discussion

Hyperelastic properties or coefficients of the exponential stress-strain relation were reported from bi-axial tests performed on bovine heart samples by previous researchers. However, the stress-strain curves showed various Young's modulus from 2-7 KPa to 150 KPa. The average Young's modulus for muscle strips of rats' left ventricular walls tested in biaxial was reported as 30 KPa. This number increased from 100 to 300 KPa for human hearts with increasing collagen content. The results obtained from using finite element

analysis were from 4 to 100 KPa. Effective shear stiffness of 10-15 KPa was reported from magnetic resonance elastography performed in vivo on pigs. However, much higher stiffness coefficients were found in the fiber direction (2.6 GPa) from ultrasonic velocity measurement on freshly excised ovine hearts. Based on the above results, it was concluded that there is a considerable variation between the reported moduli, which caused by the difference in sample preparation methods and the condition of the sample such as the specific parts of the heart that it was obtained, the time window between the extraction of the heart from the body and testing, and whether it was extracted from human, bovine, rat, or pig body. [21]

Although some aspects of the passive mechanical responses of the myocardium are well characterized using bi-axial testing, more accurate methods need to be used for detailed materials parameter estimations for constitutive laws that are used for modeling the human myocardium. In this study, we tried to obtain more accurate results by using the finite element method. The average Young's modulus and shear stiffness were measured in this study on the isolated sheep left and right ventricular wall tissue. The following chart demonstrates the results obtained in this research. The obtained results were in the same range as those reported in the literature on animals or humans, with the average Young's modulus of 146.33 and 83.5 KPa in the x and y-direction. The shear stiffness is also calculated in this study with an average amount of 11.6 Kpa, which also is in the range of the results calculated in the previous study. The Young's modulus is higher in the x-direction showing that the specimens have higher stiffness in that direction caused by the direction of the fibers. Moreover, Young's modulus is higher in the left ventricles; however,

the shear modulus is almost the same in both ventricles and slightly higher through the left ventricle.

Furthermore, we tried to calculate Young's modulus along the fibers and in the cross-fiber direction. The obtained results demonstrated that the specimens have considerably higher stiffness along the fibers followed by lower displacement in that direction. These results explained the underlying fact that we obtained a higher value for Young's modulus in the X-direction compared to Y-direction, as the fibers were aligned more horizontally.

Table 4.6 Comparison of the moduli of the images.

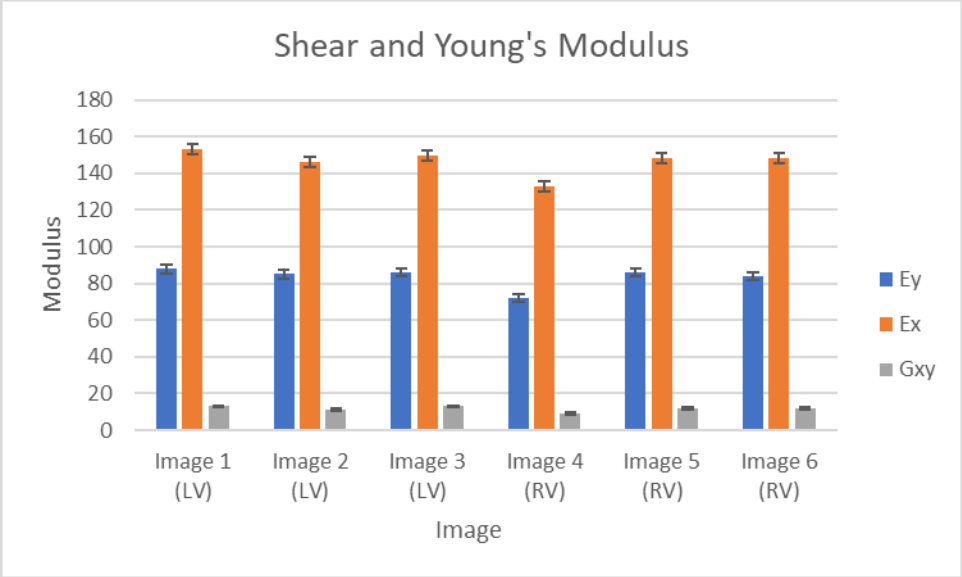

The relationship found between Young's modulus and the collagen content is the basis of the development of an indirect tool for evaluating the effects of the tissue composition on the cardiac tissue's mechanical properties. The amount of collagen in the tissue is one factor contributing to tissue compliance, and the mechanical properties of the heart tissue enhanced by increasing the collagen content. The following chart shows that

the collagen content is higher in the left ventricle, and Young's modulus increases by increasing the collagen content. Additionally, it was shown that the shear stiffness does not show a considerable correlation with the collagen content variation and the amount of the shear modulus is almost the same in the specimens obtained from both ventricles. Although, it is slightly higher in the left ventricle. These results agree with the previous research demonstrating that the collagen amount has significant effects on the mechanical properties of the heart tissue. However, the correlation between the amount of collagen and Young's modulus is more complicated, and the variation of the other content, such as glycosaminoglycans and elastin, also influences the properties of the cardiac tissue and more studies have to be done to find a more reliable relationship between the heart tissue's mechanical properties and the collagen content.

Table 4.7 Correlation between collagen ratio and the moduli

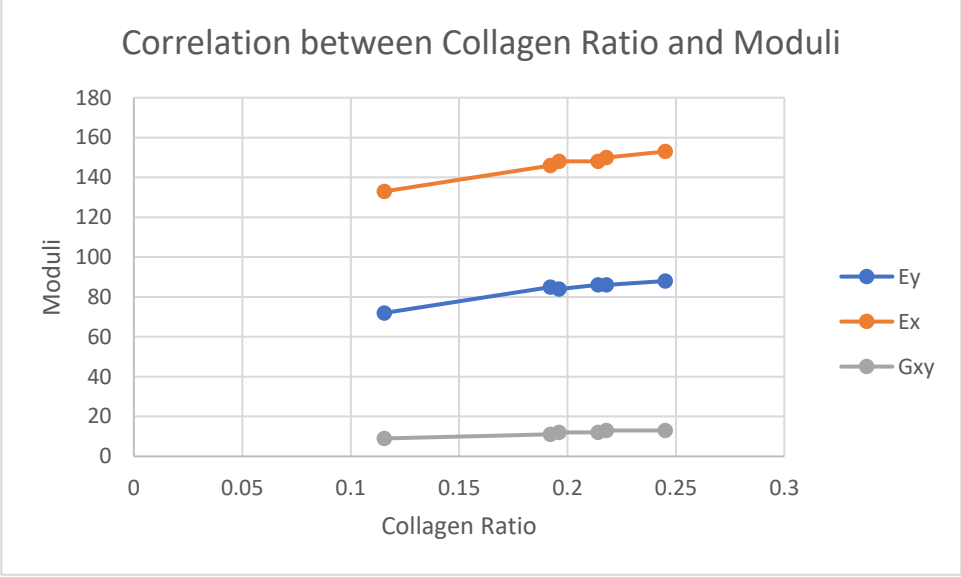

There were some limitations to this study that warrant further investigations. The limited number of tissue samples was due to the difficulty of accessing the previous results. Another limitation is related to the methods used for modeling the heart tissue; In this study, we used a two-dimensional model, and we consider each content as a homogenous material. For a better result, we need to use a three-dimensional model, enabling us to consider a geometry for the specimen and find the effect of the geometry on the heart tissue's mechanical properties. The myocytes tissue should also be considered a slightly compressible hyperelastic material with relatively soft properties that demonstrate different young's modulus during a cardiac cycle.

Based on the points mentioned in this chapter, utilizing finite element methods for obtaining the cardiac tissue's mechanical properties has been proven to be accurate and precise. However, the application of combining the image processing methods and finite element analysis on the images obtained from the heart tissue remains challenging, but the feasibility was shown. Thus, our method could be transferred to an in-vivo study. The mechanical properties determined by the combination of image processing and finite element analysis could be compared to the mechanical properties determined from experimental methods. Furthermore, the correlation of collagen along with elastin and glycosaminoglycans can be studied more precisely.

CHAPTER 5: CONCLUSION AND RECOMMENDATION

In this project, we tried to combine finite element modeling and image processing of the images from left and right ventricles obtained from a healthy ovine heart to determine the shear modulus and Young's modulus of the cardiac tissue. In the first step, we divided the images into three sections which are collagen, non-collagenous EMC, and myocytes. Then, we allocated specific mechanical properties to each part; The collagen fibers behavior was represented by isotropic linear elastic with large displacement to simulate the large strains occurring during the ventricles filling. Myocytes are also considered an isotropic material. We applied three different loading conditions to calculate the specimens' mechanical properties: tensile stress in the x and y direction and shear stress and studied the heart tissue behavior. We used the obtained data to calculate Young's modulus's average value in the x and y direction, Poisson’s ratio, and the shear stiffness. In the final step, we used the above data to calculate the constitutive matrices of each specimen. Based on the results and discussion presented in the preceding sections, the following calculation can be drawn:

1. Young's modulus in the x and y direction is almost identical with the mean value of 83.5 KPa in the y-direction and 146.33 KPa in the x-direction, which agrees with the previous studies. However, the mean value is slightly higher in the x-direction associating with the lower displacement, demonstrated that the obtained specimens

have higher stiffness in that direction causing by the collagen fibers orientation. Furthermore, Young's modulus is higher through the left ventricle in both directions demonstrating the underlying fact that the left ventricle has a higher amount of collagen, leading to higher stiffness.

2. The shear strain was calculated by applying shear stress on the sides. The obtained results are in the range of the previous studies, with a mean value of 11.6 KPa. The results show that the shear stiffness is almost the same in both ventricles. Moreover, the calculation of the shear stiffness is more complicated than tensile stiffness, and further investigation needs to be conducted on this subject. It may result from the fact that we consider all contents (collagen, non-collagenous EMC, and myocytes) as isotropic materials, resulting in a discrepancy in the results.

3. We tried to calculate Young's modulus along the fibers and in the cross-fiber direction. The obtained results demonstrated that the specimens have considerably higher stiffness along the fibers followed by lower displacement in that direction. This result explained the underlying fact that we obtained a higher value for Young's modulus in the X-direction compared to Y-direction, as the fibers were aligned more in the x-direction.

Additionally, we tried to find a correlation between the collagen content variation and the heart tissue's mechanical properties. The amount of collagen in the tissue is one factor contributing to tissue compliance, and the mechanical properties of the heart tissue enhanced by increasing the collagen content. Based on the previous chapter results, it was shown that Young's modulus of the ventricles increased with increasing the collagen

content both in x and y-direction. Moreover, it was shown that the shear stiffness does not show a considerable correlation with the variation in the collagen content, and its amount remains almost the same for all specimens. Additionally, the collagen content is higher through the left ventricle leading to a higher Young's modulus. However, the correlation between the collagen content and the heart tissue's mechanical properties is more complicated, and further studies are needed to understand its effects better. Moreover, the variation of the other contents, such as elastin and glycosaminoglycans, should also be considered.

In conclusion, understating the mechanical properties of the heart tissue and its behavior under different strain-stress conditions is the basis of studying the heart's performance. We could diagnose heart diseases more accurately with a precise and complete understanding of heart performance and its microstructure variation within different heart regions. There have been so many scientists who tried to find a method for calculating cardiac tissue's mechanical properties. Although, it remains a challenging area and there is a considerable variation between the reported moduli, which caused by the difference in sample preparation methods and the condition of the sample such as the specific parts of the heart that it was obtained, the time window between the extraction of the heart from the body and testing, and whether it was extracted from human, bovine, rat, or pig body. Previous studies mainly focused on conducting research using biaxial testing. However, several drawbacks are associated with using this method, including variation in the mechanical properties' values according to the experimental loading conditions. The proposed method is a promising tool for evaluating mechanical properties within the left

and right ventricular myocardium using finite element modeling. We can calculate the heart tissue's mechanical behavior based on our data while reducing the errors associated with conducting research using biaxial testing methods.

The future step in this study is to consider the exact geometry of the left and right ventricle by conducting a three-dimensional model of the heart tissue. Another limitation to this study is the small number of samples. We need to perform more experiments in order to establish a viable trend in the data. Moreover, we can improve our results by considering the myocytes as a slightly compressible hyperelastic material with relatively soft properties that demonstrate different young's modulus during a cardiac cycle. Another source of error is the fact that we only considered a single value for the applied force; However, the applied force on the ventricle is not constant, and it changes during one cardiac cycle, so for more accurate results, we should study the heart behavior under different applied forces within one cardiac cycle. More importantly, we have to use images obtained by in vivo methods such as MRI as the heart properties and behavior change considerably immediately after death.

LIST OF REFERENCE

1. Chandran, K.B., Rittgers, S.E. and Yoganathan, A.P., 2012. *Biofluid mechanics: the human circulation*. CRC press.

2. Tu, J., Inthavong, K. and Wong, K.K.L., 2015. *Computational Hemodynamics–Theory, Modelling, and Applications*. Springer.

3. Miller, C., 2020. 14.3 Heart. *Human Biology*.
4. Kleinstreuer, C., 2006. *Biofluid Dynamics: Principles and selected applications*. CRC Press.

5. Javani, S., 2016. *Regional Mechanical Properties and Microstructure of Ovine Heart Chambers.*

6. Sadraddin, H.L., 2019. *Antiarrhythmic effect of human bone marrow-derived CD271+ mesenchymal stem cells tested in vivo using a new infarction-re-infarction mouse model* (Doctoral dissertation, Universität Rostock).

7. Burkoff, D., 2002. *Mechanical properties of the heart and its interaction with the vascular system. Cardiac Physiology,* 46, pp.1-23.

8. Pawlina, W. and Ross, M.H., 2018. *Histology: a text and atlas: with correlated cell and molecular biology*. Lippincott Williams & Wilkins.

9. Mescher, A. L. (2013). Junqueira's *Basic Histology (13th ed.).* New York, NY: McGraw-Hill Education.

10. Kumar, V., Abbas, A. K., Aster, J. C. (2013). Robbins *Basic Pathology (9th ed.).* Philadelphia, PA: Elsevier Saunders.

11. Suckow, M.A., Hankenson, F.C., Wilson, R.P. and Foley, P.L. eds., 2019. *The laboratory rats*. Academic Press.

12. Demer, L.L. and Yin, F.C., 1983. *Passive biaxial mechanical properties of isolated canine myocardium.* The Journal of Physiology, 339(1), pp.615-630.

13. Novak, V.P., Yin, F.C.P. and Humphrey, J.D., 1994. *Regional mechanical properties of passive myocardium.* Journal of biomechanics, 27(4), pp.403-412.

14. Gao, H., Li, W.G., Cai, L., Berry, C. and Luo, X.Y., 2015. *Parameter estimation in a Holzapfel–Ogden law for healthy myocardium. Journal of engineering mathematics,* 95(1), pp.231-248.

15. Holzapfel, G.A. and Ogden, R.W., 2009. Constitutive modeling of passive myocardium: a structurally based framework for material characterization. *Philosophical Transactions of the Royal Society A: Mathematical, Physical and Engineering Sciences*, 367(1902), pp.3445-3475.

16. Wang, H.M., Gao, H., Luo, X.Y., Berry, C., Griffith, B.E., Ogden, R.W. and Wang, T.J., 2013. Structure-based finite strain modeling of the human left ventricle in diastole. *International Journal for numerical methods in biomedical engineering*, 29(1), pp.83-103.

17. Palit, A., Bhudia, S.K., Arvanitis, T.N., Turley, G.A. and Williams, M.A., 2018. *In vivo estimation of passive biomechanical properties of human myocardium.* Medical & biological engineering & computing, 56(9), pp.1615-1631. Vcqc1

18. Cook, R.D., 2007. *Concepts and applications of finite element analysis*. John Wiley & sons.

19. Gonzalez, R.C., 2004. *Digital Image Processing Using Matlab*. Gonzalez Woods & Eddins. Pdf. Education.

20. Hassaballah, A.I., Hassan, M.A., Mardi, A.N. and Hamdi, M., 2013. *An inverse finite element method for determining the tissue compressibility of the human left ventricular wall during the cardiac cycle.* Plos One, 8(12), p.e82703.

21. Périé, D., Dahdah, N., Foudis, A. and Curnier, D., 2013. *Multi-parametric MRI is an indirect evaluation tool of the mechanical properties of in-vitro cardiac tissues. BMC cardiovascular disorders,* 13(1), pp.1-9.

22. Perotti, L.E., Ponnaluri, A.V., Krishnamoorthi, S., Balzani, D., Ennis, D.B. and Klug, W.S., 2017. *Method for the unique identification of hyper-elastic material properties using full-field measures. Application to the passive myocardium material response. International Journal for numerical methods in biomedical engineering,* 33(11), p.e2866.

23. https://en.wikipedia.org/wiki/Cardiac muscle.

24. Asner, L., Hadjicharalambous, M., Chabiniok, R., Presutti, D., Sammut, E., Wong, J., Carr-White, G., Chowienczyk, P., Lee, J., King, A. and Smith, N., 2016. *Estimation of passive and active properties in the human heart using 3D tagged MRI. Biomechanics and modeling in mechanobiology,* 15(5), pp.1121-1139.

25. Davidson JM, Hill KE, Mason ML, Giro MG. *Longitudinal gradients of collagen and elastin gene expression in the porcine aorta*. J Biol Chem 1985; 260:1901–8.

26. Yang, P.C., and Clancy, C.E., 2012. In silico prediction of sex-based differences in human susceptibility to cardiac ventricular tachyarrhythmias. *Frontiers in physiology*, *3*, p.360.

27. Suckow, M.A., Hankenson, F.C., Wilson, R.P. and Foley, P.L. eds., 2019. *The laboratory rat*. Academic Press.

28. Pope, A.J., Sands, G.B., Small, B.H. and LeGrice, I.J., 2008. *Three-dimensional transmural organization of perimysial collagen in the heart*. American Journal of Physiology-Heart and Circulatory Physiology, 295(3), pp.H1243-H1252.

29. Pope, A.J., Sands, G.B., Smaill, B.H., LeGrice, I.J., 2008. *Three-dimensional transmural organization of perimysial collagen in the heart.* Am. J. Physiol. Heart Circ. Physiol., 295, H1243–h1252.

30. Deshmukh, M. and Bhosle, U., 2011. A survey of image registration. *International Journal of Image Processing (IJIP)*, *5*(3), p.245.

31. Wang, C., Chen, M., Zhao, J.M. and Liu, Y., 2011. *Fusion of color Doppler and magnetic resonance images of the heart.* Journal of digital imaging, 24(6), pp.1024-1030.

32. Weber, K.T., Sun, Y., Tyagi, S.C. and Cleutjens, J.P., 1994. *Collagen network of the myocardium: function, structural remodeling, and regulatory mechanisms*. Journal of molecular and cellular cardiology, 26(3), pp.279-292.

33. Fan, D., Takawale, A., Lee, J. and Kassiri, Z., 2012. *Cardiac fibroblasts, fibrosis, and extracellular matrix remodeling in heart disease. Fibrogenesis & tissue repair*, 5(1), pp.1-13.

34. Villarreal, F. ed., 2005. *Interstitial fibrosis in heart failure* (Vol. 253). Springer Science & Business Media.

35. Kania, G., Blyszczuk, P. and Eriksson, U., 2009. *Mechanisms of cardiac fibrosis in inflammatory heart disease. Trends in cardiovascular medicine,* 19(8), pp.247-252.

36. Yabluchanskiy, A., Ma, Y., Chiao, Y.A., Lopez, E.F., Voorhees, A.P., Toba, H., Hall, M.E., Han, H.C., Lindsey, M.L. and Jin, Y.F., 2014. *Cardiovascular and Cerebrovascular Aging–New Mechanisms and Insights: Cardiac aging is initiated by matrix metalloproteinase-9-mediated endothelial dysfunction.* American Journal of Physiology-Heart and Circulatory Physiology, 306(10), p.H1398.

37. Lin, J., Lopez, E.F., Jin, Y., Van Remmen, H., Bauch, T., Han, H.C. and Lindsey, M.L., 2008. Age-related cardiac muscle sarcopenia: *Combining experimental and mathematical modeling to identify mechanisms. Experimental gerontology*, 43(4), pp.296-306.

38. López, B., González, A., Hermida, N., Valencia, F., de Teresa, E. and Díez, J., 2010. *Role of lysyl oxidase in myocardial fibrosis: from basic science to clinical aspects*. American Journal of Physiology-Heart and Circulatory Physiology, 299(1), pp.H1-H9.

39. Arvidsson, P.M., Töger, J., Carlsson, M., Steding-Ehrenborg, K., Pedrizzetti, G., Heiberg, E. and Arheden, H., 2017. *Left and right ventricular hemodynamic forces in healthy volunteers and elite athletes assessed with 4D flow magnetic resonance imaging*. American Journal of Physiology-Heart and Circulatory Physiology, 312(2), pp.H314-H328.

40. Alkhouli, N., Mansfield, J., Green, E., Bell, J., Knight, B., Liversedge, N., Tham, J.C., Welbourn, R., Shore, A.C., Kos, K. and Winlove, C.P., 2013. *The mechanical properties of human adipose tissues and their relationships to the structure and composition of the extracellular matrix*. American Journal of Physiology-Endocrinology and Metabolism, 305(12), pp.E1427-E1435.

41. McCain, M.L., Yuan, H., Pasqualini, F.S., Campbell, P.H. and Parker, K.K., 2014. Matrix elasticity regulates the optimal cardiac myocyte shape for contractility. *American Journal of Physiology-Heart and Circulatory Physiology*, *306*(11), pp.H1525-H1539.

42. Black, L.D., Allen, P.G., Morris, S.M., Stone, P.J. and Suki, B., 2008. Mechanical and failure properties of extracellular matrix sheets as a function of structural protein composition. *Biophysical journal*, *94*(5), pp.1916-1929.

43. Jacot, J.G., Martin, J.C. and Hunt, D.L., 2010. Mechanobiology of cardiomyocyte development. *Journal of biomechanics*, *43*(1), pp.93-98.

44. Thomas, V.S., Lai, V. and Amini, R., 2019. A computational multi-scale approach to investigate mechanically induced changes in tricuspid valve anterior leaflet microstructure. *Acta biomaterialia*, *94*, pp.524-535.

45. Fomovsky, G.M., Thomopoulos, S. and Holmes, J.W., 2010. Contribution of extracellular matrix to the mechanical properties of the heart. *Journal of molecular and cellular cardiology*, *48*(3), pp.490-496.

46. Avazmohammadi, R., Li, D.S., Leahy, T., Shih, E., Soares, J.S., Gorman, J.H., Gorman, R.C. and Sacks, M.S., 2018. An integrated inverse model-experimental approach to determine soft tissue three-dimensional constitutive parameters: Application to post-infarcted myocardium. *Biomechanics and modeling in mechanobiology*, *17*(1), pp.31-53.

47. Li, D.S., Avazmohammadi, R., Merchant, S.S., Kawamura, T., Hsu, E.W., Gorman III, J.H., Gorman, R.C., and Sacks, M.S., 2020. Insights into the passive mechanical behavior of left ventricular myocardium using a robust constitutive model based on full 3D kinematics. *Journal of the mechanical behavior of biomedical materials*, *103*, p.103508.

APPENDICES

Appendix A: Young's Modulus and Poisson's Ratio Matrices

Left ventricle:

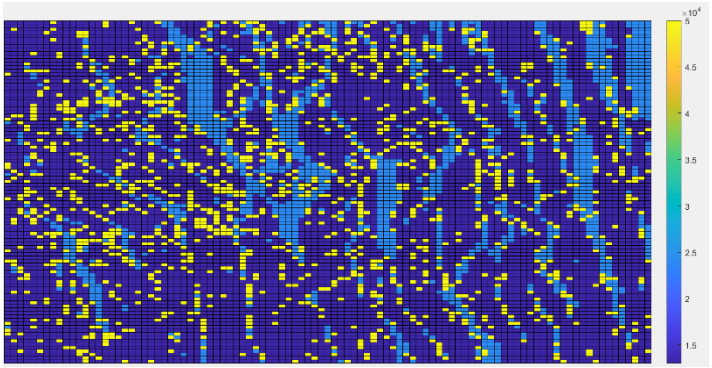

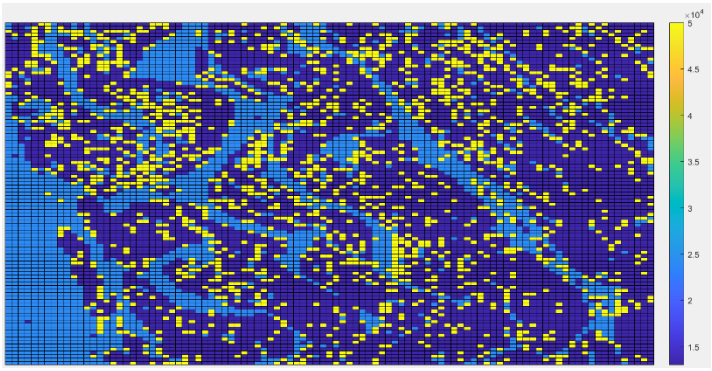

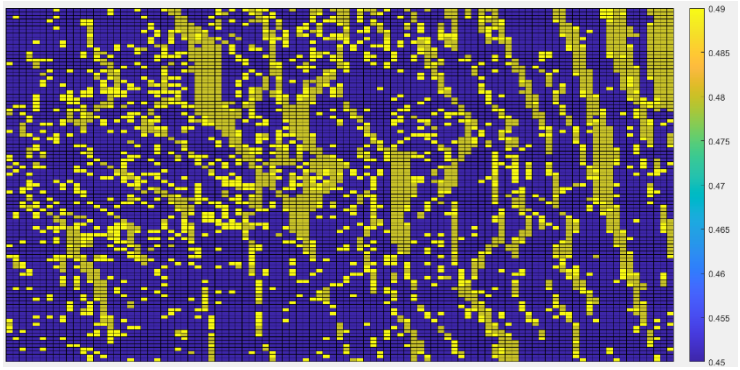

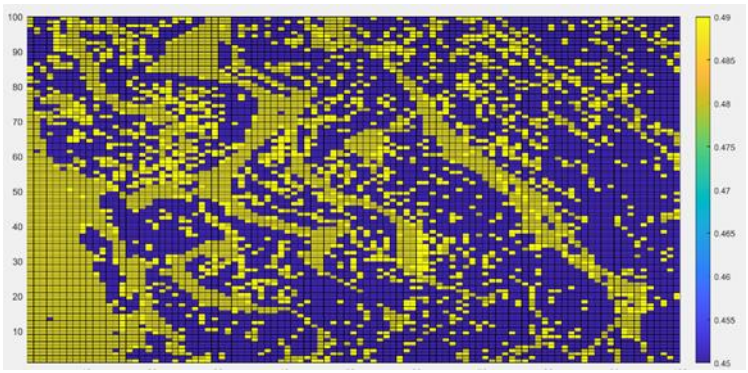

Right Ventricle:

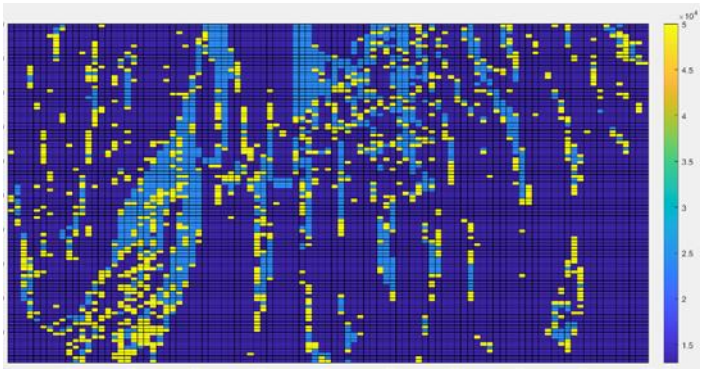

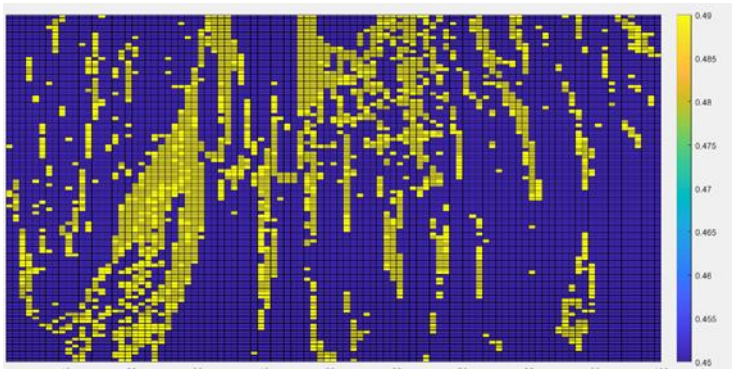

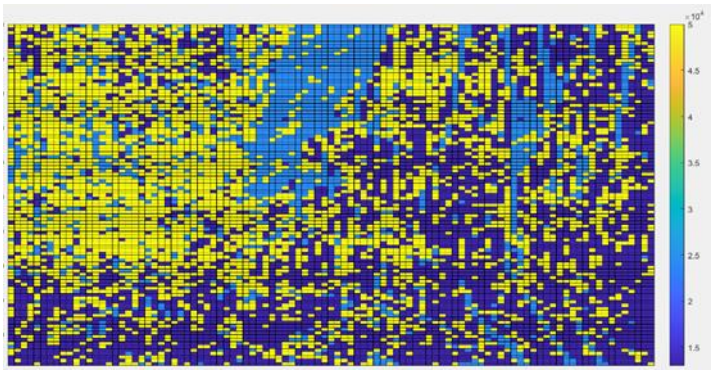
×10^-4
5
4.5
4
3.5
3
2.5
2
1.5

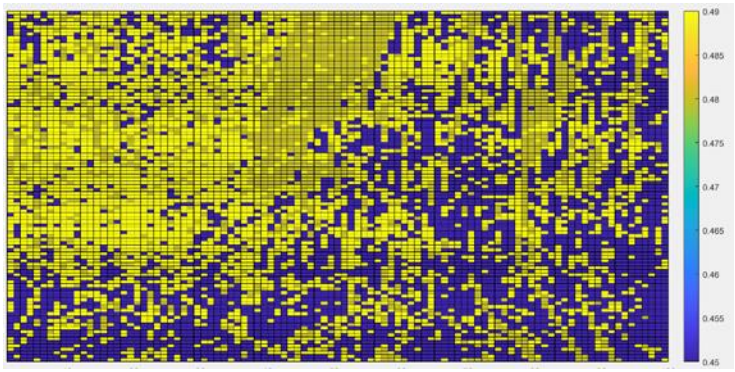
0.49
0.485
0.48
0.475
0.47
0.465
0.46
0.455
0.45

Appendix B: Deformed and Initial Structure of the Samples Under Loading Conditions

Tensile loading:

Left ventricle:

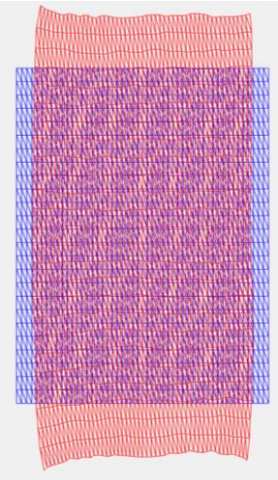

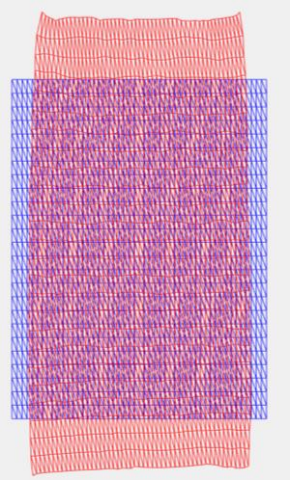

Right ventricle

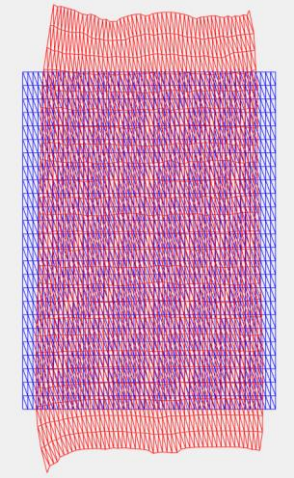

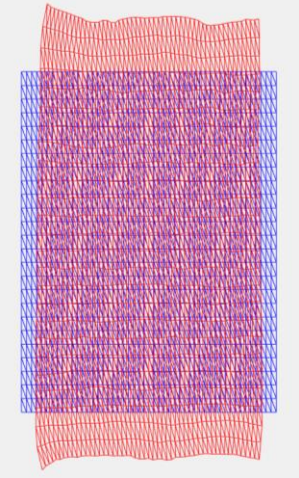

Tensile loading

Left ventricle:

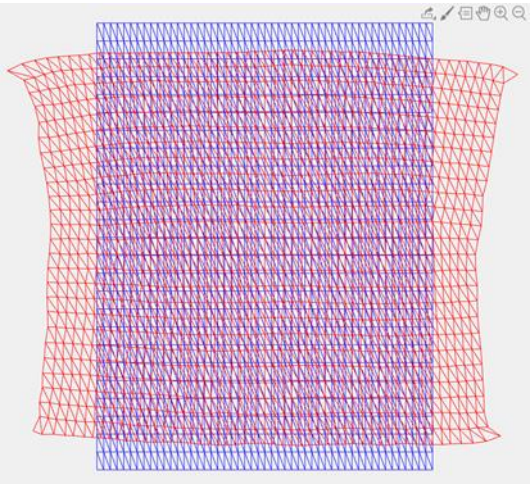

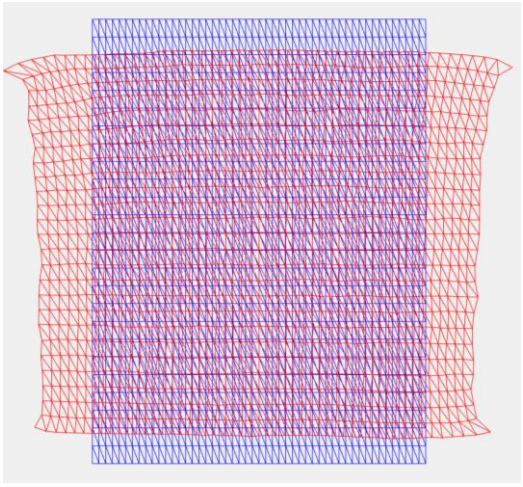

Right ventricle:

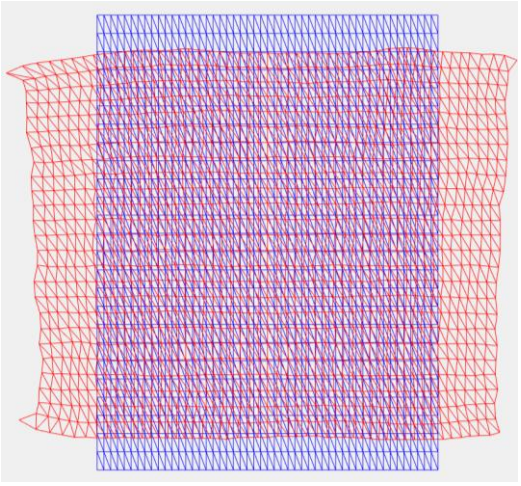

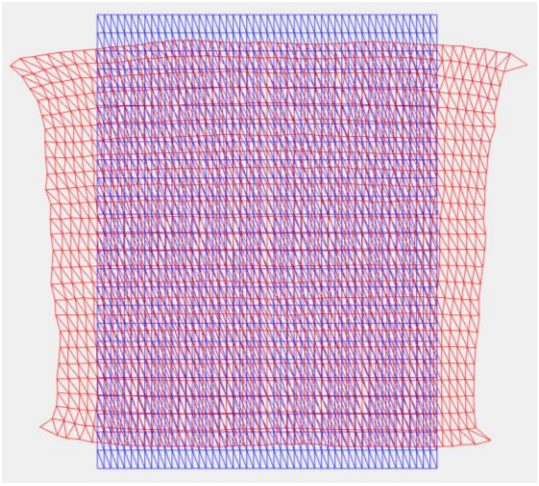

Shear loading

Left ventricle:

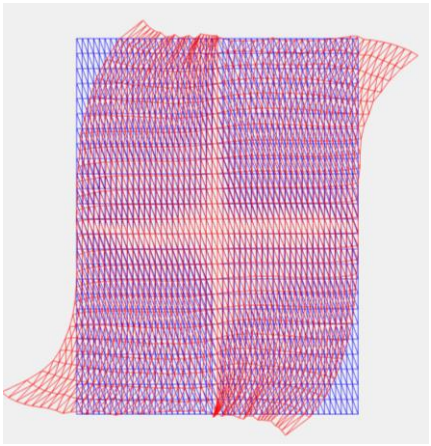

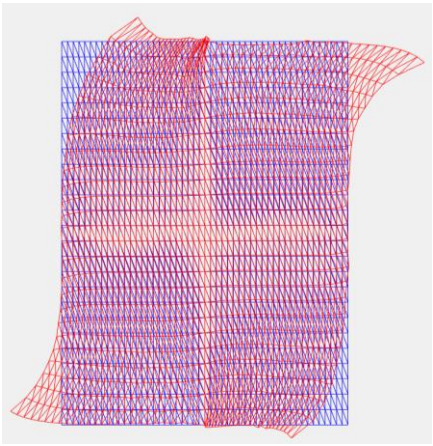

Right ventricle:

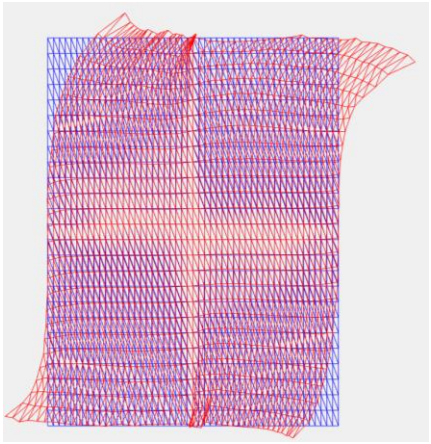

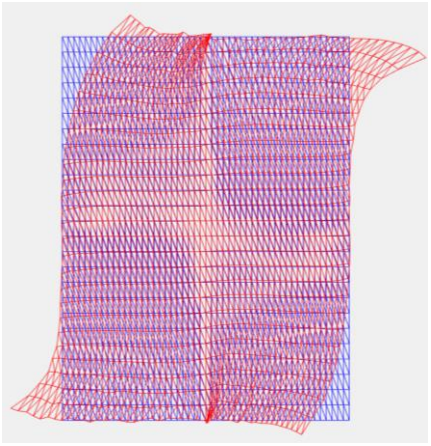

Appendix C: Developed Codes in MATLAB

```
%========== mesh generation ======================
 t=1;  %y
 L=0.75;     %x
 n=25;    % nodes in y direction
 m=25;     % nodes in x direction=2*m
node=T6_NodeCoord(L,m,t,n); %nodes
elem=T6_DefE(m,n);            %elements
Plot_Element(elem,node);
%========== initialization =============
%tarndfering the matrix to a 100*100 matrix
a=rgb2gray(f);
b= a;
d=[];
e=[];
n=12;
m=16;
z=600/n;
x=800/m;
      for l=1:z
          for k=1:x
              e=b(n*(l-1)+1:n*l,m*(k-1)+1:m*k);
              d(l,k)=sum(e(:))./(n*m);
          end
      end
% allocating the Young's modulus and poisson's ratio
 v=d;
v(v<=190 & v>=118)= 2.25e3; %E for fat
v(v<=100 & v>=20)= 13e3;   % E for myocytes
v(v<=118 & v>=100)= 50e3; %E for collagen
s=d;
s(s<=190 & s>=118)= 0.4; %nu for fat
s(s<=100 & s>=20)= 0.45;   % nu for myocytes
```

```
s(s<=118 & s>=100)= 0.49; %nu for collagen
E= v;    %Young's modulus
nu= s;  %Poission's ratio
% plotting the Young's modulus mattix
figure (1)
pcolor(E)
% plotting the Poisson's ratio mattix
figure (2)
pcolor(nu)
% Definig the applied load and boundary conditions
F0= 0.4;          % applied force
left=[];
right=[];
top=[];
bottom=[];
symmetry=[];
symmetry2=[];
for i=1:size(node,1)
    if (node(i,1)>L-0.0001); right=[right,i]; end
    if(node(i,1)<0.0001); left=[left, i]; end
    if(node(i,2)>t-0.0001); top=[top,i]; end
    if (node(i,2)<0.0001); bottom=[bottom,i]; end
    if (node(i,2)<0.0001 && node(i,1)<0.0001); tip=i; end
    if(node(i,1)>L-0.0001 &&node(i,2)>t-0.001); tip1=i; end
    if(node(i,1)>L-0.0001 && node(i,2)<t-0.001); tip2=i; end
    if(node(i,1)<L-0.00001  && node(i,2)>t-0.0001);tip3 =i; end
    if(node(i,1)<0.00001  && node(i,2)<0.0001); tip4=i; end
    if(node(i,2)>t/2-0.0001 && node(i,2)<t/2+0.0001); symmetry=[symmetry,i]; end
    if (node(i,1)>L/2-0.0001 && node(i,1)<L/2+0.0001); symmetry2=[symmetry2,i];end
end
```

```
elem_num=size(elem,1);           %total element number
node_num=size(node,1);           %total node number
K=zeros(node_num*2,node_num*2);  %stiffness matrix
U=zeros(node_num*2,1);           %displacement vector
F=zeros(node_num*2,1);           %force vector
%bc: degrees of freedom with zero displacement
bc=[symmetry*2,symmetry2*2-1]; %fixed
%F: external forces. format: F(degree of freedom)=nodal magnitude
F(right*2-1)= F0;
F(left*2-1)= -F0;
F(top*2)= F0;
F(bottom*2)= -F0;
F(left*2)=-F0;
F(right*2)=F0;
%========== element assembly ==========
%C=E/(1-nu*nu)*[1,nu,0;nu,1,0;0,0,0.5-0.5*nu];    %plane stress
for i=1:50
  for j=1:50
C{i+(j-1)*50}=E(i,j)/((1-nu(i,j))*nu(i,j))*[1,nu(i,j),0;nu(i,j),1,0;0,0,0.5-0.5*nu(i,j)]; %plane stress
        end
end
  for i=1:elem_num
  Ke{i}=zeros(12,12);
   m=elem(i,:);
    n=[2*m(1)-1, 2*m(1), 2*m(2)-1, 2*m(2), ...
       2*m(3)-1, 2*m(3), 2*m(4)-1, 2*m(4),2*m(5)-1,2*m(5),2*m(6)-1,2*m(6)];
nodeC=node(elem(i,:),:);     %coordinates of the nodes of the element
 Ke{i}=T6_SME(nodeC,t,C{i}); % stiffness matrix of the element
    K(n,n)=K(n,n)+Ke{i} ;
  end
```

```
% Calculation of the displacement
dof=1:(2*node_num);
dof(bc)=[];
F(bc)=[];
K(bc,:)=[];
K(:,bc)=[];
U(dof)=inv(K)*F;
Ux=U(1:2:end);
Uy=U(2:2:end);
%========== compute stress and strain ============
 for i=1:elem_num
 n=[2*elem(i,1)-1 2*elem(i,1) 2*elem(i,2)-1 2*elem(i,2) 2*elem(i,3)-1 2*elem(i,3) ...
 2*elem(i,4)-1 2*elem(i,4) 2*elem(i,5)-1 2*elem(i,5) 2*elem(i,6)-1 2*elem(i,6)]; % degrees of freedom of element i
 DispE=U(n); % nodal displacements of the element
 nodeC=node(elem(i,:),:); % coordinates of the nodes of the element
 stressE=T6_Stress(C{i},nodeC,DispE); % stresses at all nodes of the element
 StressG(i,:)=stressE;
 end
 % Average for nodes
StressR=zeros(node_num,6); % Initial global stress matrix by nodes
for i=1:node_num
 StressR(i,1:3)=zeros(3,1);
 count=0;
 for j=1:elem_num;
 if ismember(i,elem(j,:));
 count=count+1;
 [~,index]=ismember(i,elem(j,:)); % get index in element j of node i
 StressR(i,1:3)=StressR(i,1:3)+StressG(j,[3*index-2 3*index-1 3*index]); % get sum
 end;
 end;
```

```
 StressR(i,1:3)=StressR(i,1:3)/count; % average
 StressR(i,4)=0.5*(StressR(i,1)+StressR(i,2))+0.5*sqrt((StressR(i,1)-StressR(i,2))^2+4*StressR(i,3)^2); % max main normal stress
 StressR(i,5)=0.5*(StressR(i,1)+StressR(i,2))-0.5*sqrt((StressR(i,1)-StressR(i,2))^2+4*StressR(i,3)^2); % min main normal stress
 StressR(i,6)=0.5*(StressR(i,4)-StressR(i,5)); % max tangential stress
end;
for i=1: elem_num
    Strain(i,:)=(StressR(i,1:3)/C{i})';
end
% plottinf the defromed and initial structures
scale=1.0/max(abs(U))*0.2;
Deformed (0,node,elem,scale,U,StressR);
```